



HAL
open science

Engineering of Tunable Allosteric-like Fluorogenic Protein Sensors

Fanny Broch, Lina El Hajji, Nicolas Pietrancosta, Arnaud Gautier

► **To cite this version:**

Fanny Broch, Lina El Hajji, Nicolas Pietrancosta, Arnaud Gautier. Engineering of Tunable Allosteric-like Fluorogenic Protein Sensors. ACS Sensors, 2023, 8 (10), pp.3933-3942. 10.1021/acssensors.3c01536 . hal-04243996

HAL Id: hal-04243996

<https://hal.sorbonne-universite.fr/hal-04243996>

Submitted on 16 Oct 2023

HAL is a multi-disciplinary open access archive for the deposit and dissemination of scientific research documents, whether they are published or not. The documents may come from teaching and research institutions in France or abroad, or from public or private research centers.

L'archive ouverte pluridisciplinaire **HAL**, est destinée au dépôt et à la diffusion de documents scientifiques de niveau recherche, publiés ou non, émanant des établissements d'enseignement et de recherche français ou étrangers, des laboratoires publics ou privés.



Distributed under a Creative Commons Attribution - NonCommercial - NoDerivatives 4.0 International License

Engineering of Tunable Allosteric-Like Fluorogenic Protein Sensors

Fanny Broch,^[a] Lina El Hajji,^[a] Nicolas Pietrancosta^[a,b] & Arnaud Gautier^{*,[a,c]}

[a] Sorbonne Université, École Normale Supérieure, Université PSL, CNRS, Laboratoire des Biomolécules, LBM, 75005 Paris, France

[b] Neuroscience Paris Seine-Institut de Biologie Paris Seine (NPS-IBPS) INSERM, CNRS, Sorbonne Université, Paris, France

[c] Institut Universitaire de France

* Correspondence should be sent to: arnaud.gautier@sorbonne-universite.fr

KEYWORDS: *Allosteric protein sensors • Chemogenetic fluorescent reporters • Analyte sensing • Optical sensors*

ABSTRACT: Optical protein sensors that enable to detect relevant biomolecules of interest play central roles in biological research. Coupling fluorescent reporters to protein sensing units has enabled the development of a wide range of biosensors that recognize analytes with high selectivity. In these sensors, analyte recognition induces a conformational change of the protein sensing unit that can modulate the optical signal of the fluorescent reporter. Here, we explore various designs for the creation of tunable allosteric-like fluorogenic protein sensors through incorporation of sensing protein units within the chemogenetic fluorescence-activating and absorption-shifting tag (FAST) that selectively binds and stabilizes the fluorescent state of 4-hydroxybenzylidene rhodanine (HBR) analogs. Conformational coupling allowed us to design analyte-responsive optical protein sensors through allosteric-like modulation of fluorogen binding.

Detection and quantification of analytes involved in biological processes require the design of reliable biosensors, coupling fluorescent reporters to analyte-specific binding domains, interacting proteins, or enzyme target-sequences. Initially based on fluorescent proteins (FPs), these sensors are either intensimetric, when relying on a single FP (illustrated by calcium ion detection with GCaMP and its improved variants¹⁻³) or ratiometric, where a conformational change of the chimeric protein influences the Förster Resonance Energy Transfer (FRET) efficiency between two FPs (notably leveraged for glutamate imaging^{4,5}). The recent addition of chemogenetic probes, comprised of a synthetic fluorescent moiety coupled to a genetically encoded part, has provided new opportunities for the design of innovative biosensor with a hybrid nature.⁶ Relying on resonance energy transfer, the coupling of self-labelling protein HaloTag with SNAP-tag⁷, a bioluminescent luciferase⁸ or a fluorescent protein⁹ has provided detection tools for a wide range of molecules. Cellular apposition and long-term contact have been visualized using fluorescence-activating proteins (FAPs) targeted by a heterobivalent ligand.^{10,11} Usual protein engineering strategies are now supported by computer-based structural and functional predictions, that notably allowed de novo design of fluorogenic Ca²⁺ biosensors, in which ligand detection regulates chromophore binding to mini-FAP, and thus fluorescence.¹² Such allosteric control has been illustrated as well by coupling HaloTag to various sensing modalities that undergo conformational change and influence the fluorescent state equilibrium of the bound fluorophore.¹³

Allosteric regulation is a widespread process for modulating protein function and regulating cell signaling and metabolism. Binding of a ligand at one site of an allosteric protein positively or negatively affects the output function of a distant binding or catalytic site through a conformational change. This design principle can be applied to the construction of allosterically regulated protein switches in which proteins with input and output functions of interest are combined such that their functions are significantly coupled^{14,15}, opening new avenues for the design of artificial protein switches for imaging, diagnostic and therapeutic applications.^{16,17}

The chemogenetic fluorescence-activating and absorption-shifting tag (FAST) represents an interesting reporter for the creation of optical protein sensors. This protein tag selectively and non-covalently binds and stabilizes the fluorescent state of fluorogenic chromophores (so-called fluorogens), which are otherwise dark when free in solution or in cells, including hydroxybenzylidene rhodanine (HBR) derivatives.^{18,19} FAST and its variants can be used to monitor gene expression and protein localization in live cells and organisms under aerobic^{18,20-25} and anaerobic conditions.²⁶⁻³⁰ Inserting circularly permuted (cp)FAST between the Ca²⁺-binding Calmodulin and the peptide M13 allowed the monitoring of Ca²⁺ fluxes in live cells by fluorescence microscopy.³¹ Dynamic interactions between proteins could be probed in live cells through fusion to two complementary fragments of FAST³². Further engineering recently allowed the generation of a fluorogenic chemically induced proximity tool to control and visualize the proximity of fusion

proteins.³³ These developments suggested that fusion of sensing protein units undergoing conformational change upon analyte recognition with FAST could create analyte-responsiveness by conditioning fluorogen complexation, thus fluorescence, through allosteric-like coupling.

FAST is an attractive reporting module for the design of fluorescent sensors: first, its small size should permit the coupling to sensing protein domains with minimal perturbation of their folding. Second, FAST and its engineered variants form fluorescent assemblies with HBR derivatives¹⁹ and alternative fluorogenic push-pull chromophores with spectral properties covering the entire visible spectrum.^{20,25} This tunability conveniently enables control over the spectral properties, providing higher design versatility than FPs. These variants also display various fluorogen affinities (and potentially conformational sensitivity), providing options for the optimization and tuning of conformational coupling between the chromophore binding pocket and an analyte recognition domain.

Here, we explore various strategies for the design of allosteric-like fluorogenic protein sensors based on FAST and show that insertion of sensing protein domains into FAST or its derivatives enables to create responsiveness to various biological analytes.

Results and Discussion

Evaluation of Allosteric Coupling in Fluorogenic Protein Sensor

In allosteric fluorogenic sensors, the binding of the analyte can either raise or lower the binding affinity of the fluorogen, leading to positive or negative allosteric modulation of fluorescence. The cooperativity constant $\alpha = K_{D,F} / K_{D,F/A}$ (where $K_{D,F}$ is the binding affinity constant of F (the fluorogen) in absence of A (the analyte), and $K_{D,F/A}$ is the binding affinity constant of F when A is already bound to the sensor) enables to know if the cooperativity is positive ($\alpha > 1$), or negative ($\alpha < 1$) (see the full model in **Text S1**, **Fig. S1** and **Fig. S2**). The case $\alpha = 1$ indicates that the fluorogen and the analyte bind the sensor independently. In allosteric sensors, the influence between the two ligands is reciprocal, therefore the binding of the fluorogen modifies the binding affinity of the analyte. The binding affinity of the analyte is thus characterized by an apparent dissociation constant $K_{D,app}$ that depends on the fluorogen concentration (see **Fig. S1**, **Fig. S2** and **Text S1**). Consequently, the concentration of fluorogen can be advantageously adjusted to tune the binding affinity of the analyte (vide infra).

Engineering of Positive Glutamate-Responsiveness

To test the idea of engineering analyte-responsive FAST, we first envisioned coupling FAST with a glutamate sensing unit. Glutamate plays a key role both intracellularly and in chemical

communication in the nervous system.^{34,35} As sensing domain, we used the glutamate/aspartate import solute-binding protein (GltI) from *E. coli*. The design of ratiometric FRET glutamate sensors through insertion of GltI between two fluorescent proteins suggested that GltI undergoes conformational change upon glutamate binding.³⁶ This was further supported by the generation of intensimetric glutamate sensors through insertion of a circularly permuted GFP (cpGFP) in between residues 253 and 254 of GltI.³⁷ A circularly permuted version of GltI (cpGltI) has been recently generated by connecting the N and C termini with a linker of 37 amino acids and by reinstating termini at position 253 and 254,³⁸ further expanding the potential of GltI for the creation of glutamate-responsiveness. To generate glutamate-responsive FAST, we tested the insertion of GltI(5-279) into FAST (in between residues 114 and 115) or its circular permutation cpFAST (in between residues 125 and 1), yielding Glu-FAST-1 and Glu-FAST-2. We also inserted FAST or cpFAST into GltI (in between residues 253 and 254), leading to Glu-FAST-3 and Glu-FAST-4. The existence of cpGltI allowed us to generate the circular permutations of these four topologies (cpGlu-FAST-(1-4)). The eight proteins were expressed in bacteria and purified for subsequent in vitro characterization. Through titrations with the fluorogen HMBR in absence and in presence of 5 mM glutamate, we found that Glu-FAST-2 was the topology in which HMBR binding was the most allosterically coupled to glutamate binding (**Fig. S3** and **Table S1**). Glutamate binding increased HMBR affinity by 2.2-fold, showing that Glu-FAST-2 exhibited positive cooperativity (**Fig. 1a-d,i**).

To determine the glutamate affinity of Glu-FAST-2, we measured fluorescence in presence of 1 μ M HMBR and glutamate concentrations ranging from 0.5 μ M to 250 μ M. Note that the concentration of HMBR was chosen approximately equal to $(K_{D,HMBR} \cdot K_{D,HMBR/glutamate})^{1/2}$, as this concentration is a good compromise to have both a good dynamic range and an acceptable fluorescence signal (see **Fig. S4** for more details). Fitting of the glutamate titration curve yielded an apparent $K_{D,app}$ for glutamate binding of 7 μ M, a value within the range expected to be relevant for biosensing applications in physiological conditions. In these conditions, the fluorescence dynamic range of Glu-FAST-2, i.e. the maximal fluorescence variation of the sensor, was 1.8-fold. Glutamate-responsiveness could be further enhanced by several steps of protein engineering (**Fig. S5** and **Table S2**). Through the combined insertion of a rigid Pro-Pro linker between GltI and the N-terminal fragment of FAST (FAST(1-114) = NFAST) and truncation of the first residue of the C-terminal fragment of FAST (CFAST), we generated Glu-FAST-2.1, which exhibits a 4.3-fold higher affinity for HMBR in presence of glutamate. At 1 μ M HMBR, Glu-FAST-2.1 exhibits a $K_{D,app}$ for glutamate binding of 6 μ M and an improved fluorescence dynamic range (2.5-fold vs 1.8-fold for Glu-FAST-2), in agreement with an increased positive allosteric-like modulation (**Fig. 1e-g**).

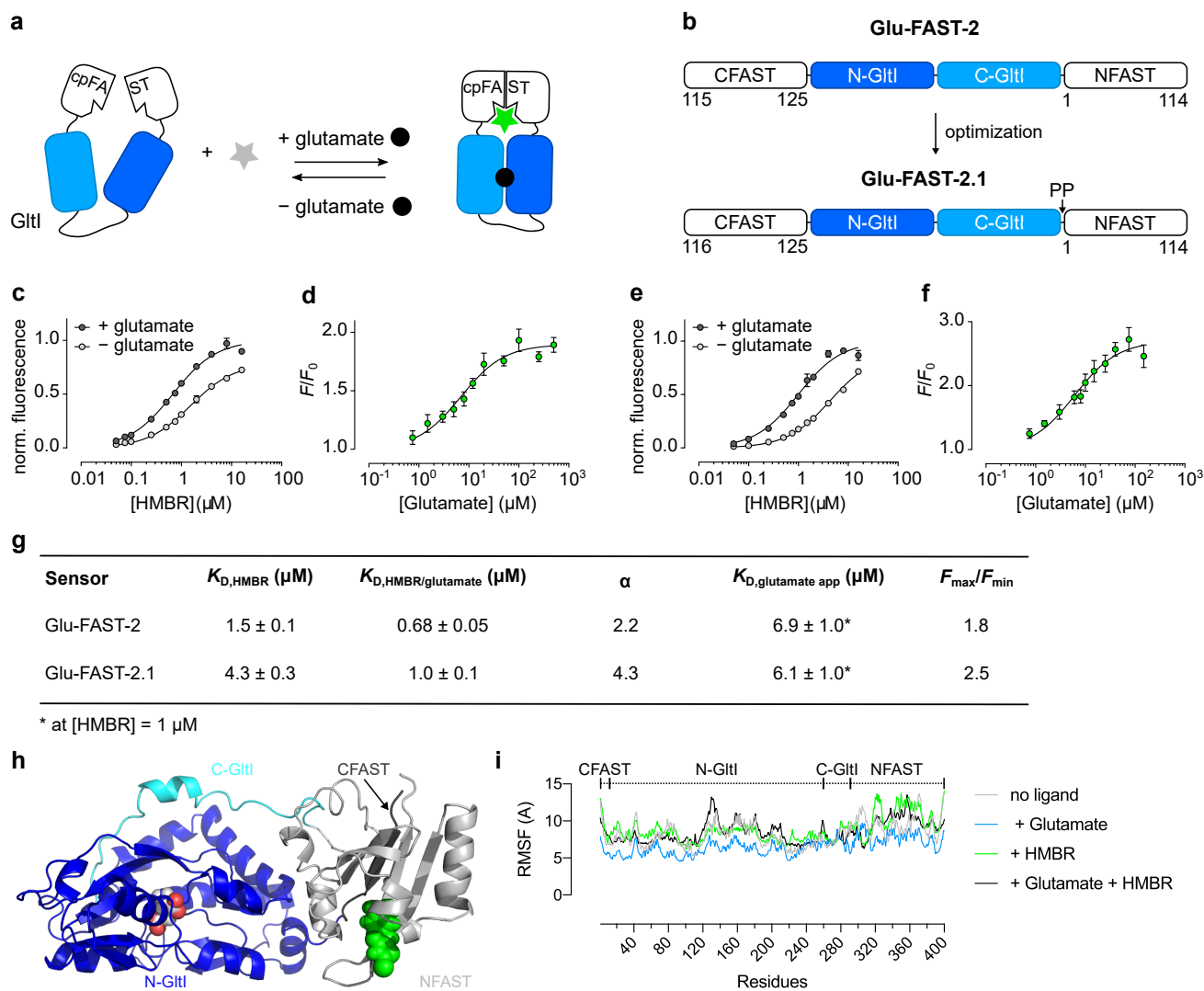


Figure 1. FAST-based glutamate sensors. (a) Principle of glutamate-responsiveness. (b) Topology of the selected biosensor Glu-FAST-2 and its optimized version, Glu-FAST-2.1. (c,e) HMBR titration curves of Glu-FAST-2 and Glu-FAST-2.1, respectively, in the absence (light grey) and in the presence of 5 mM glutamate (dark grey) in pH 7.4 HEPES buffer (50 mM) containing NaCl (150 mM). (d,f) Glutamate titration curves of Glu-FAST-2 and Glu-FAST-2.1, respectively, in the presence of 1 μM HMBR. Data represent the mean \pm sem ($n = 3$). The least-squares fit (line) gave the thermodynamic dissociation constants $K_{D,HMBR}$, $K_{D,HMBR/glutamate}$ and $K_{D,glutamate\ app}$ provided in (g). The sensor concentration was fixed at 0.1 μM . (g) The dissociation constant of the fluorogen is given in the absence ($K_{D,HMBR}$) and in the presence of glutamate ($K_{D,HMBR/glutamate}$), and the cooperativity constant α is calculated as the ratio of the dissociation constant in the absence and in presence of glutamate ($K_{D,HMBR}/K_{D,HMBR/glutamate}$). The apparent dissociation constant $K_{D,glutamate\ app}$ for glutamate binding is also given with the associated fluorescence intensity increase observed upon analyte addition (F_{max}/F_{min}). (h) Structural model of Glu-FAST-2.1 bound to glutamate and HMBR generated by homology modeling and molecular dynamics. GluI is in blue and FAST in grey. HMBR and glutamate are shown in space-filling model. (i) Root mean square fluctuations (RMSF) of the residues of Glu-FAST-2.1 during molecular dynamic simulations of 30 ns (see also Fig. S5).

To get insights about the functioning of Glu-FAST-2.1, we generated atomic resolution models by homology modeling, further refined by molecular dynamics. Our modeling suggests that Glu-FAST-2.1 do not undergo strong conformational

change in presence of its ligands in agreement with the modest dynamic range of the sensor (Fig. 1h,i and Fig. S6a-g). Nevertheless, fine analysis of the root mean square fluctuations (RMSF) of each residue during long (30 ns) molecular

dynamics showed that the conformational dynamics of the protein sensor is significantly different when the binding sites are empty, occupied by one of the two ligands, or occupied by both ligands (**Fig. 1i** and **Fig. S6a-g**). We observed in particular that the binding of glutamate reduces the conformation dynamics of both the GltI and the FAST domains, in agreement with a cooperative conformational coupling between the two domains. The effect of the binding of HMBR was less pronounced but changes in the conformational dynamics could be observed through changes of the residue RMSF profile (**Fig. S6a-g**) in agreement with a conformational coupling between the FAST and GltI domains. In addition, estimation of the sensor-ligand binding energy using docking simulations suggested that the affinity for HMBR increases when the glutamate is already bound and that, reciprocally, the affinity for glutamate increases when HMBR is already bound (**Fig. S6h,i**), in agreement with an allosteric-like coupling.

Engineering of Positive K⁺-Responsiveness

To further evaluate the incorporation of analyte responsiveness into FAST, we coupled FAST to the bacterial potassium binding protein (Kbp),³⁹ previously used for the design of ratiometric FRET-based, as well as intensimetric single fluorescent protein-based potassium ions (K⁺) indicators.^{40,41} As the most abundant intracellular cations, K⁺ ions are essential for proper cell functions and membrane potential.⁴² In presence of K⁺, Kbp adopts a globular structure with its N- and C- termini close to each other, while *ab initio* model of apo-Kbp suggested that Kbp adopts an elongated conformation in absence of K⁺ with quite distant N- and C-termini.³⁹ As for the generation of glutamate-responsive FAST, we tested different topologies to identify a K⁺-responsive FAST. First, insertion of Kbp into FAST (in between residues 114 and 115) and cpFAST (in between residues 125 and 1) yielded K⁺-FAST-1 and K⁺-FAST-2. We also tested insertion of FAST and cpFAST in between the K⁺ binding domain (BON) and the lysine motif (Lys) of Kbp, yielding K⁺-FAST-3 and K⁺-FAST-4. The four proteins were expressed in bacteria and purified for subsequent in vitro characterization (**Fig. S7** and **Table S3**). Titrations with the fluorogen HMBR in absence and in presence of 10 mM K⁺ showed that HMBR binding was allosterically coupled to K⁺ binding into K⁺-FAST-2 with a cooperativity constant $\alpha = 2.3$ (**Fig. 2a-d,g**). The three other topologies showed no significant allosteric coupling.

Fluorescence measurements in presence of 0.1 μ M HMBR and K⁺ concentrations ranging from 0.025 mM to 25 mM enabled us to determine a $K_{D,app}$ for K⁺ of 0.15 mM and a fluorescence dynamic range of 1.9-fold for this sensor (**Fig. 2d,g**). The affinity of K⁺-FAST-2 for K⁺ ions approached the affinity of Kbp alone, previously determined by isothermal titration calorimetry (ITC).³⁹ As the affinity of K⁺-FAST-2 for K⁺ ions was too high to consider any applications in biosensing, we inserted a 15-residues flexible linker between the BON and Lys domains

within K⁺-FAST-2 to lower the affinity for K⁺. This strategy was previously shown to reduce K⁺ affinity.⁴⁰ Accordingly, the resulting K⁺-FAST-5 exhibited an eight-fold greater $K_{D,app}$ for K⁺ binding, reaching a range of affinity more suitable for biosensing applications (**Fig. S8** and **Table S4**). The subsequent N-terminal truncation of cFAST reduced the affinity of the biosensor for HMBR in the K⁺-bound and -free state, further reducing the affinity for K⁺ and improving the dynamic range. In agreement with a positive allosteric coupling between the K⁺ and HMBR binding sites, the optimized K⁺-FAST-5.1 exhibits a higher $K_{D,app}$ for K⁺ binding of 2 mM at 0.1 μ M HMBR, and undergoes a 2.2-fold fluorescence increase upon K⁺ binding (**Fig. 2e-g**).

To get insights about the functioning of K⁺-FAST-5.1, we generated atomic resolution models by homology modeling, further refined by molecular dynamics. As for Glu-FAST-2.1, our modeling suggests that K⁺-FAST-5.1 do not undergo strong conformational change in presence of its ligands in agreement with the modest dynamic range of the sensor (**Fig. 2h,i** and **Fig. S9a-g**). Detailed analysis of the root mean square fluctuations (RMSF) of each residue during long (30 ns) molecular dynamics showed that the conformational dynamics of the protein sensor are significantly different when the binding sites are empty, occupied by one of the two ligands, or occupied by both ligands (**Fig. 2i** and **Fig. S9a-g**). We observed in particular that the binding of either K⁺ or HMBR reduces the conformation dynamics of both the Kbp and the FAST domains (**Fig. S9a-g**), in agreement with a reciprocal cooperative conformational coupling between the two domains. In addition, estimation of the sensor-ligand binding energy using docking simulations suggested that the affinity for HMBR increases when K⁺ is already bound and that, reciprocally, the estimated affinity for K⁺ increases when HMBR is already bound (**Fig. S9h,i**), in agreement with an allosteric-like coupling.

Engineering of Negative ATP-Responsiveness

Encouraged by the generation of positive glutamate- and K⁺-responsiveness through allosteric coupling, we next explored the incorporation of ATP responsiveness into FAST. ATP is considered to be the “energy currency” of the cell and is essential for most cellular processes. As ATP sensing protein domain, we used the ϵ -subunit of FoF₁-ATP synthase from the thermophilic *Bacillus* PS3 (*B. PS3* ϵ), which can adopt either a ligand-free extended conformation, or a hairpin-like contracted conformation upon ATP binding.^{43,44} This ATP-induced conformational change has been used for the design of ATP protein sensors through coupling with a fluorescent reporter.⁴⁵⁻⁴⁷ Allosteric-like coupling with FAST was thus considered either by insertion of *B. PS3* ϵ into FAST or cpFAST, yielding ATP-FAST-1 and ATP-FAST-2 respectively, or by inserting FAST or cpFAST in *B. PS3* ϵ at position 107-110 (previously identified as functional split site),⁴⁸ yielding ATP-FAST-3 and ATP-FAST-4, respectively. Through titrations with

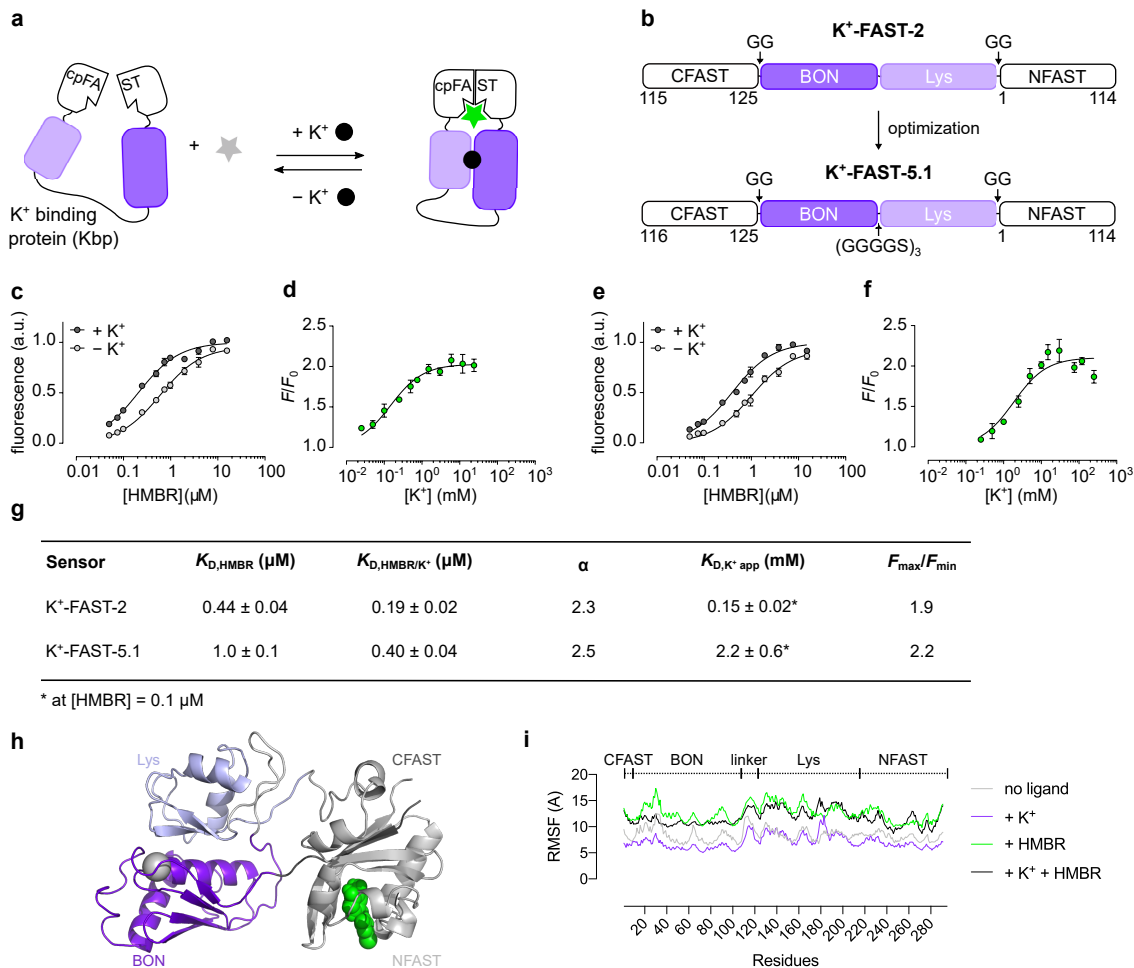


Figure 2. FAST-based K⁺ sensors. (a) Principle of K⁺-responsiveness. (b) Topology of the selected biosensor K⁺-FAST-2 and its optimized version, K⁺-FAST-5.1. (c,e) HMBR titration curves of K⁺-FAST-2 and K⁺-FAST-5.1, respectively, in the absence (light grey) and in the presence (dark grey) of 10 mM and 100 mM K⁺, respectively, in pH 7.4 HEPES buffer (50 mM) containing MgCl₂ (75 mM). (d,f) K⁺ titration curves of K⁺-FAST-2 and K⁺-FAST-5.1, respectively, in the presence of 0.1 μM HMBR. Data represent the mean \pm sem ($n = 3$). The least-squares fit (line) gave the thermodynamic dissociation constants $K_{D,HMBR}$, $K_{D,HMBR/K^+}$ and $K_{D,K^+ \text{ app}}$ provided in (g). The sensor concentration was fixed at 0.1 μM . (g) The dissociation constant of the fluorogen is given in the absence ($K_{D,HMBR}$) and in the presence of K⁺ ($K_{D,HMBR/K^+}$), and the cooperativity constant α is calculated as the ratio of the dissociation constant in the absence and in presence of K⁺ ($K_{D,HMBR}/K_{D,HMBR/K^+}$). The apparent dissociation constant $K_{D,K^+ \text{ app}}$ for K⁺ binding is also given with the associated fluorescence intensity increase observed upon analyte addition ($F_{\text{max}}/F_{\text{min}}$). (h,i) Structural model of K⁺-FAST-5.1 bound to K⁺ and HMBR generated by homology modeling and molecular dynamics. Kbp is in purple and FAST in grey. HMBR and K⁺ are shown in space-filling model. (i) Root mean square fluctuations (RMSF) of the residues of K⁺-FAST-5.1 during molecular dynamic simulations of 30 ns.

the fluorogen HMBR in absence or presence of 5 mM ATP, we found that ATP binding reduced HMBR affinity for all four topologies, demonstrating negative binding cooperativity (Fig. S10 and Table S5). We observed the strongest allosteric-like coupling in ATP-FAST-1 and ATP-FAST-2. In these two chimeric proteins, ATP binding led to 100-fold and 25-fold reduction of HMBR affinity, respectively (i.e. $\alpha = 0.01$ and 0.04

respectively). Interestingly, we found that HMBR was binding ATP-free ATP-FAST-1 and ATP-FAST-2 with dissociation constants $K_{D,HMBR}$ very close to those found within FAST and cpFAST respectively (Fig. 3a-c,f, Fig. S10 and Table S5). This result suggested that FAST and cpFAST were properly folded in absence of ATP in ATP-FAST-1 and ATP-FAST-2, and that the ATP-induced conformational transition of *B. PS3* ϵ domain

induced a conformational change of FAST and cpFAST causing the observed HMBR affinity drop.

As ATP-FAST-1 exhibited the strongest allosteric coupling, we next characterized its affinity for ATP. We measured green fluorescence at a fixed HMBR concentration and ATP concentrations ranging from 5 μM to 5000 μM . We chose $[\text{HMBR}] = 1 \mu\text{M}$ as a good compromise to obtain large dynamic range and acceptable fluorescence. We observed a 8.3-fold decrease of fluorescence upon ATP binding, and determined that ATP-FAST-1 bound ATP in a highly selective manner with a $K_{D,\text{app}}$ of 0.23 mM (**Fig. 3e-f** and **Fig. S11a**). The large fluorescence dynamic range was further confirmed by measuring the excitation and emission spectra of ATP-FAST-1 in absence and presence of ATP (**Fig. 3g**). In agreement with a strong allosteric coupling between FAST and *B. PS3 ϵ* , we observed that an increase of HMBR concentration induced an increase of the $K_{D,\text{app}}$ for ATP binding, demonstrating that the binding affinity of ATP could be modulated by changing the fluorogen concentration (**Fig. S12a**). The negative cooperativity of ATP-FAST-1 was further indirectly confirmed by creating ATP-unresponsiveness. Introduction of the mutations R122K/R126K known to reduce ATP binding to *B. PS3 ϵ* ⁴³ generated an ATP-insensitive ATP-FAST-1 variant whose high affinity for HMBR was unaffected by ATP (**Fig. S13a,b**).

The properties of ATP-FAST-1 were further modulated by using various HBR analogs. One remarkable feature provided by the hybrid nature of FAST is the ability to modify its spectral properties by simply changing the fluorogen. In addition to HMBR that forms green fluorescent assembly with FAST, the use of HBR-3,5DM and HBR-3,5DOM yields yellow and orange-red fluorescent assemblies, respectively.¹⁹ We found that ATP-FAST-1 exhibited ATP-responsiveness with HBR-3,5DM and HBR-3,5DOM, enabling to perform ATP titration with a red-shifted readout (**Fig. 3g-i**). This modularity represents an advantage over fluorescent protein-based sensors as it provides spectral versatility for multiplexed experiments without the need for reengineering the protein sensor. The use of different fluorogens also opens new ways to tune the binding affinity of ATP. As ATP-FAST-1 can bind different fluorogens, the $K_{D,\text{app}}$ for ATP binding could be modulated by using fluorogens exhibiting different binding affinities (**Fig. S12b,c**), further demonstrating the advantage of semisynthetic protein sensors.

The strong negative cooperativity of ATP-FAST-1 suggested that increasing the binding affinity of the fluorogen could significantly reduce the binding affinity of ATP, and therefore increase the $K_{D,\text{app}}$ for ATP binding. We replaced FAST with pFAST - a promiscuous FAST variant that binds a large collection of isosteric and spectrally different HBR analogs and displays > 10-fold higher affinity for most HBR analogs.²⁵ While pFAST fluorescence was confirmed to be independent from the

presence of ATP, the resulting ATP-pFAST-1 conserved a highly selective negative responsiveness to ATP and exhibited reduced ATP binding affinity (**Fig. 3d-f**, **Fig. S11b** and **Fig. S13c,d**). Through adequate choice of the fluorogen nature and concentration, it was possible to obtain ATP-responsive sensor with $K_{D,\text{app}}$ for ATP binding in the millimolar range, an affinity range that could be suitable for monitoring changes in cellular ATP levels, and a dynamic range of 6.4-fold (**Fig. S14** and **Table S6**).

To get insights about the conformational coupling between *B. PS3 ϵ* and FAST (or pFAST), we generated atomic resolution models of ATP-FAST-1 and ATP-pFAST-1 by homology modeling, further refined by molecular dynamics (**Fig. 3j-l** and **Fig. S15**). Our analysis suggested that ATP-FAST-1 and ATP-pFAST-1 can adopt two very different conformations in function of the bound ligand. In presence of ATP, *B. PS3 ϵ* adopts a closed conformation (which superimposes with the known 3D structure of *B. PS3 ϵ* bound to ATP), preventing the association of the C-terminal strand of FAST (cFAST) with the N-terminal domain (nFAST) (**Fig. 3k** and **Fig. 3l**). On the other hand, in absence of ATP and in presence of HMBR, *B. PS3 ϵ* adopts an open conformation that enables proper folding of full-length FAST (**Fig. 3j**). These two models agree with the strong negative allosteric-like coupling we observed experimentally and suggest that upon ATP binding ATP-FAST-1 and ATP-pFAST-1 undergo a strong conformational change that leads to the dissociation of cFAST and nFAST, thus preventing fluorogen binding.

To further explore the potential of the ATP-responsive FAST, we next generated sensors enabling ratiometric titration of ATP through fusion of the red fluorescent protein mCherry to the N-terminus of ATP-FAST-1 and ATP-pFAST-1. The apparent affinities of the sensors for ATP were not significantly affected by the presence of mCherry ($K_{D,\text{app}} = 89 \mu\text{M}$ for mCherry-ATP-FAST-1 and $K_{D,\text{app}} = 1.6 \text{ mM}$ for mCherry-ATP-pFAST-1 at $[\text{HMBR}] = 1 \mu\text{M}$), showing that mCherry does not interfere with the folding of the sensors. The fluorescence of mCherry remained constant upon ATP addition, enabling to normalize the fluorescent signal from HMBR (**Fig. 4a-f**). Ratiometric sensing of ATP levels could facilitate studies in biological samples and cells, by rendering measurements independent of the biosensor concentration.

Finally, we evaluated the use of our ATP sensors for the in vitro quantification of metabolites. Luminescent enzymatic assays in which a metabolite of interest is quantified through optical detection of a generic cofactor converted or formed stoichiometrically upon enzymatic conversion of the target metabolite can be a general approach for monitoring metabolites at the point of care and facilitate the diagnostic and monitoring of many diseases.⁸ We thus reasoned that our fluorogenic ATP sensor

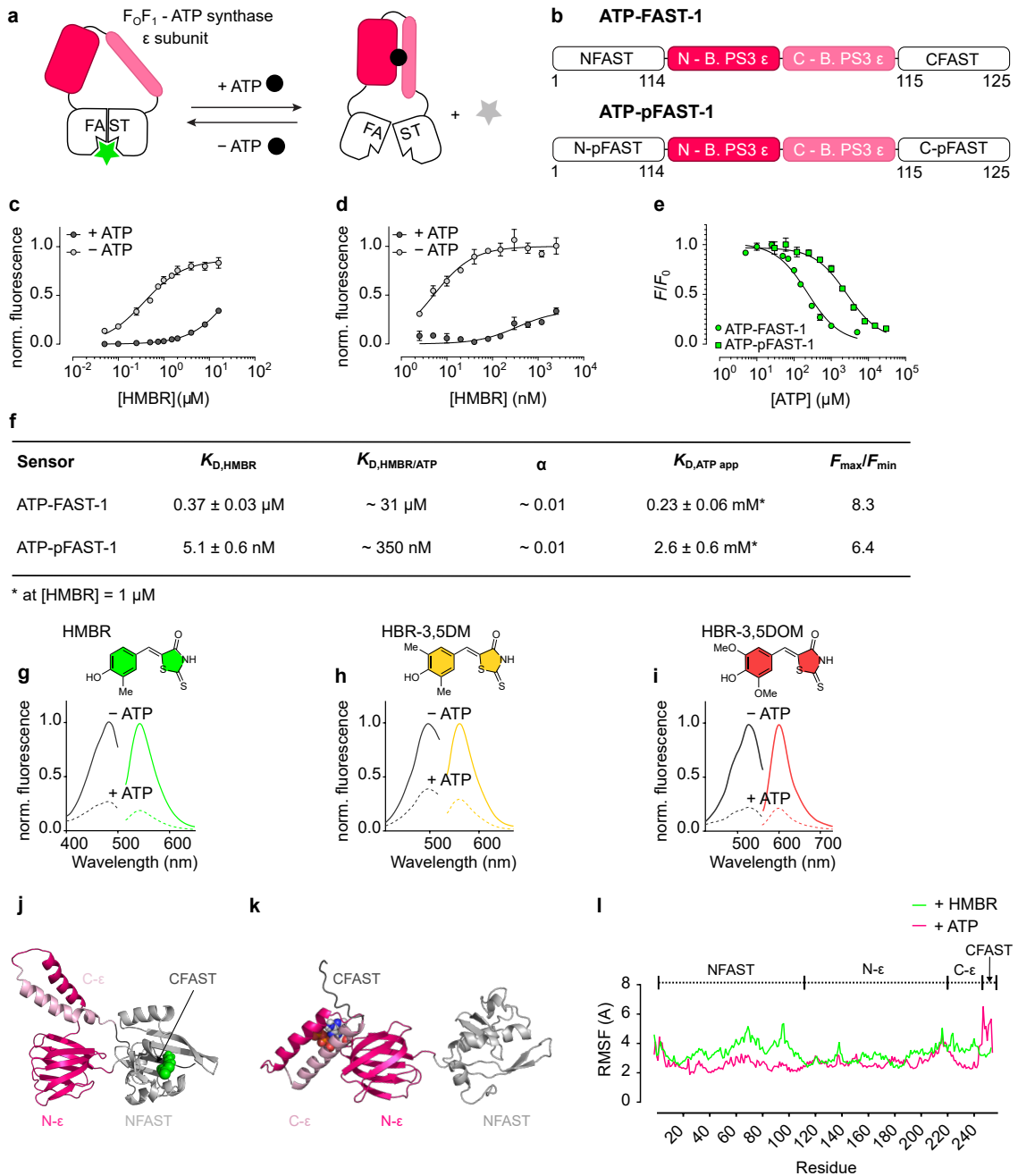


Figure 3. FAST-based ATP sensors. (a) Principle of ATP responsiveness. (b) Topology of the selected biosensor ATP-FAST-1 and ATP-pFAST-1. (c) HMBR titration curves of ATP-FAST-1 in the absence (light grey) and in the presence of 5 mM ATP (dark grey) in pH 7.4 HEPES buffer (50 mM) containing MgCl_2 (75 mM). (d) HMBR titration curves of ATP-pFAST-1 in the absence (light grey) and in the presence of 30 mM ATP (dark grey) in pH 7.4 HEPES buffer (50 mM) containing MgCl_2 (75 mM). (e) ATP titration curves of ATP-FAST-1 and ATP-pFAST-1 in pH 7.4 HEPES buffer (50 mM) containing MgCl_2 (75 mM), in the presence of $1\ \mu\text{M}$ HMBR. Data represent the mean \pm sem ($n = 3$). The least-squares fit (line) gave the thermodynamic dissociation constants $K_{D,HMBR}$, $K_{D,HMBR/ATP}$ and $K_{D,ATP\ app}$ provided in (f). The sensor concentration was fixed at $0.1\ \mu\text{M}$. (f) The dissociation constant of the fluorogen is given in the absence ($K_{D,HMBR}$) and in the presence of ATP ($K_{D,HMBR/ATP}$), and the cooperativity constant α is calculated as the ratio of the dissociation constant in the absence and in presence of ATP ($K_{D,HMBR}/K_{D,HMBR/ATP}$). The apparent dissociation constant $K_{D,ATP\ app}$ for ATP binding is also given with the associated fluorescence intensity decrease observed upon ATP addition (F_{max}/F_{min}). (g-i) Excitation and emission spectra of ATP-FAST-1 bound to HMBR, HBR-3,5DM and HBR-3,5DOM, respectively, in the absence (solid line) and in the presence (dotted line) of 5 mM ATP. The

concentration of the fluorogen was 1 μM . The sensor concentration was fixed at 0.1 μM . (j,k) Structural models of ATP-FAST-1 bound to HMBR (j) or ATP (k) generated by homology modeling and molecular dynamics. B. PS3 ϵ is in magenta and FAST in grey. HMBR and ATP are shown in space-filling model. (l) Root mean square fluctuations (RMSF) of the residues ATP-FAST-1 during molecular dynamic simulations.

should enable the design of an assay in which a metabolite of interest is phosphorylated. Fluorescence increase of our sensor upon ATP consumption could be quantified, enabling the quantification of the metabolite of interest. As a proof-of-principle, we developed an assay for the fluorometric detection of glucose for which blood monitoring is essential in the management of diabetes. Glucose can be stoichiometrically converted into 6-phosphogluconate by, first, phosphorylation by the hexokinase to form glucose 6-phosphate (G6P), consuming one ATP molecule, and then conversion of G6P into 6-phosphogluconate by the glucose-6-phosphate dehydrogenase, producing

one molecule of NADH. Measurement of the green fluorescence increase from mCherry-ATP-FAST-1 upon ATP consumption allowed us to quantify the amount of ATP used for the conversion of glucose, enabling to estimate the initial concentration of glucose (Fig. 4g). We showed that we could accurately determine glucose concentrations ranging from 150 to 420 μM . This detection range enables to envision the quantification of blood glucose concentrations, ranging from 3.9 to 7.8 mM, through 20 to 25-fold dilution of the sample.

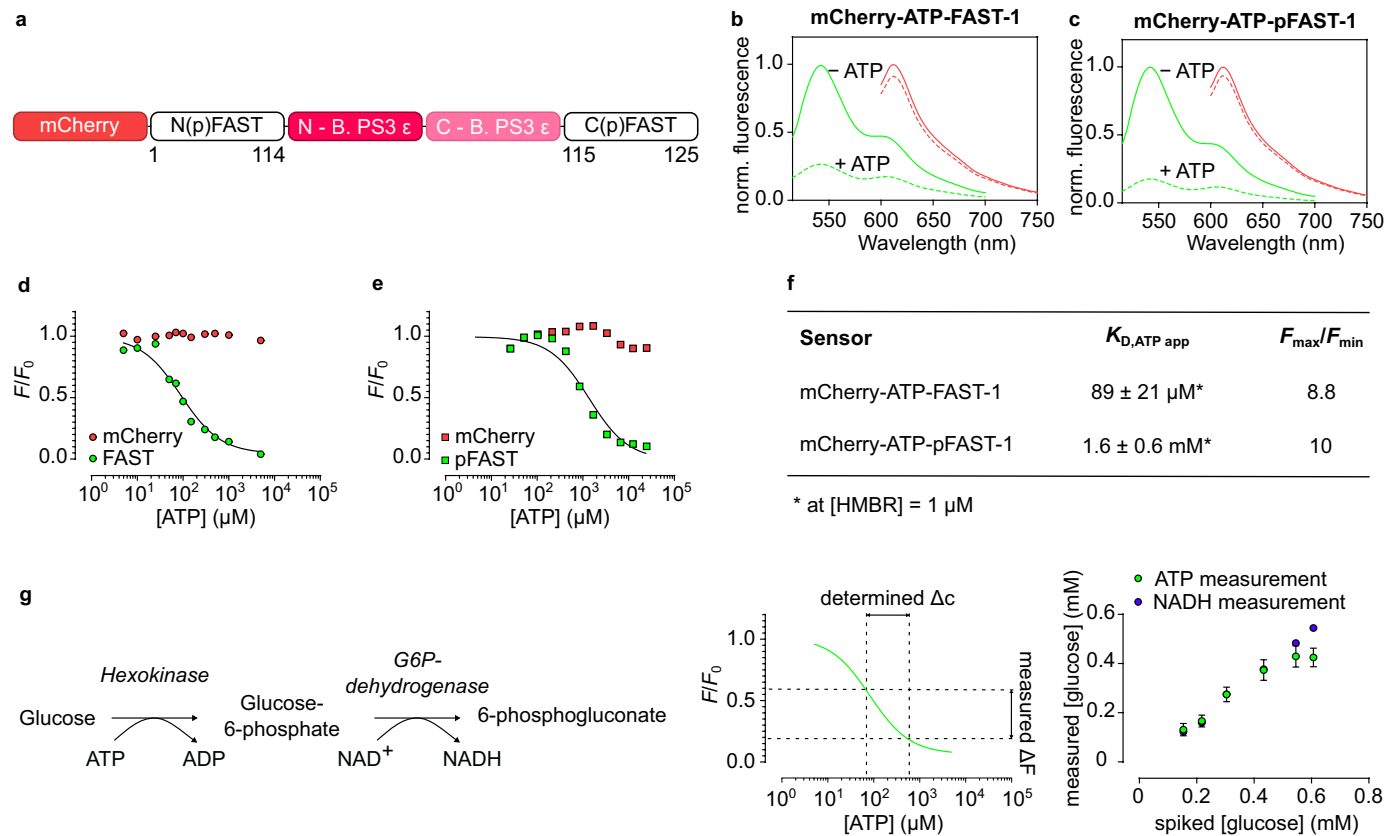


Figure 4. Ratiometric FAST-based ATP sensors. (a) Topology of the ratiometric biosensors mCherry-ATP-(p)FAST-1. (b,c) Emission spectra of mCherry-ATP-FAST-1 and mCherry-ATP-pFAST-1, respectively, at $\lambda_{ex} = 470\ \text{nm}$ (green) and $\lambda_{ex} = 555\ \text{nm}$ (red), in the absence (solid line) and in the presence of 30 mM ATP (dotted line), with 1 μM HMBR. The sensor concentration was fixed at 0.1 μM . (d,e) ATP titration curves of mCherry-ATP-FAST-1 and mCherry-ATP-pFAST-1, respectively, in pH 7.4 HEPES buffer (50 mM) containing MgCl₂ (75 mM), in the presence of 1 μM HMBR. Fluorescence intensities from HMBR and mCherry were measured at $\lambda_{ex} = 470\ \text{nm}$ (green) and $\lambda_{ex} = 555\ \text{nm}$ (red), respectively. Data represent the mean \pm sem ($n = 3$). The least-squares fit (line) gave the thermodynamic dissociation constants $K_{D,HMBR}$, $K_{D,HMBR/ATP}$ and $K_{D,ATP\ app}$ provided in (f). The sensor concentration was fixed at 0.1 μM . (f) The dissociation constant of ATP $K_{D,ATP\ app}$ in the presence of 1 μM HMBR is given with the associated fluorescence intensity decrease observed upon ATP addition

(F_{\max}/F_{\min}). (g) Quantification of a spiked glucose concentration measuring the evolution of NADH absorption or the evolution of the fluorescence intensity at $\lambda_{\text{em}} = 540$ nm using our ATP-FAST-1 sensor assay in the presence of 1 μM HMBR in pH 7.4 HEPES buffer (50 mM) containing MgCl_2 (75 mM). The sensor concentration was fixed at 0.1 μM .

Conclusion

First described in oligomeric and symmetric proteins,⁴⁹ allosteric proteins can be monomeric proteins in which two binding sites are coupled by a macromolecular conformational change induced by the binding of either ligand and having an effect on the binding of the other ligand.^{50–52} Here, we explored the design of fluorescent sensors responding to biological analytes through incorporation of various sensing units into the protein tag FAST that reversibly binds and stabilizes the fluorescent state of HBR derivatives. Our study shows that conformational coupling between FAST and a sensing domain can generate fluorescent sensors with allosteric-like behavior, in which fluorogen binding, and therefore fluorescence, is conditioned to analyte recognition.

The possibility to split FAST into two complementary fragments or to circularly permute its sequence allowed us to explore various topological designs for optimizing the conformational coupling with the sensing units. Moreover, the use of fluorogens displaying various absorption and emission spectra enabled the generation of fluorogenic sensors with various spectral properties without the need for any reengineering. The recent developments of the color tunable pFAST²⁵ and the far-red (fr)FAST²⁰ should further favor the spectral diversification and expansion of FAST-based sensors in the future. Interestingly, the apparent affinity for the analyte, and thus the range of analyte concentrations that can be measured, can be modulated through (i) change of the fluorogen concentration, (ii) use of fluorogens with different binding affinities or (iii) use of FAST variants with different fluorogen affinities, in agreement with an allosteric-like coupling between FAST and the analyte-binding domain. Our study on the incorporation of ATP-responsiveness into FAST indicates furthermore that it is possible to engineer strong allosteric-like coupling, and thus high dynamic range, if the analyte-binding protein domain undergoes a large conformational change upon analyte binding.

The design of allosteric-like fluorogenic protein sensors is still in its very early days. Before the present study, analyte-responsive fluorogenic protein sensors were only obtained through the incorporation of Ca^{2+} sensing domains in the bilirubin-based fluorescent protein UnaG⁵³ and in the *de novo* designed

mini-fluorescence-activating protein (mFAP).¹² Here, we show that the concept of allosteric-like fluorogenic protein sensors can be expanded to other analytes. In depth *in vitro* characterization allowed us to challenge the principle of allosteric-like sensors and identify the key parameters to modulate and tune their properties. This first generation of sensors can however still be improved and optimized. In particular, our FAST-based Glutamate and K^+ sensors still display rather modest dynamic range that might limit their general applicability. Future engineering will include (i) systematic engineering of the linkers (e.g. length, amino acid composition) used to connect the sensing domains and the reporter domains, and (ii) creation of new interactions between the two domains. Such engineering steps have been necessary and indispensable for the optimization of most GFP-based sensors, as engineering optimal sensors at the first attempt remains a challenge in protein engineering. Our modeling experiments will be helpful in this quest in particular to optimize the length of the linkers to be tested and identify regions within the two domains that could beneficially interact.

Future efforts should focus on (i) the implementation of such sensors for the optical monitoring of analytes of interest in live cells and organisms in real time, and (ii) the development of fluorescent or bioluminescent assays for the monitoring of metabolites at the point of care for the diagnostic and monitoring of diseases. As the binding affinity for the analyte depends on the concentration of fluorogen, the applications of such allosteric-like fluorescent sensors in live cells will require proper calibration of the intracellular concentrations of applied fluorogen, through for instance *in-cell* titration using FAST variants with known fluorogen binding affinities. In addition, the development of analyte-insensitive versions of the sensors will be useful to verify that the intracellular fluorogen concentration does not vary during the time course of the experiment.

Finally, the recent developments of powerful *de novo* protein design methods¹² and revolutionary protein structure prediction tools⁵⁴ based on artificial intelligence should accelerate and improve the overall engineering process and lead in the near future to efficient allosteric fluorogenic protein sensors for various applications in the Life sciences.

ASSOCIATED CONTENT

Supporting Information. Material and Methods, supplementary text, supplementary figures, supplementary tables, supplementary references.⁵⁵ This material is available free of charge via the Internet at <http://pubs.acs.org>.

AUTHOR INFORMATION

Corresponding Author

* E-mail: arnaud.gautier@sorbonne-universite.fr

Author Contributions

F.B., L.E.H and A.G. designed the experiments. F.B., L.E.H performed the experiments. F.B., L.E.H and A.G analyzed the experiments. N.P. performed the *in-silico* modeling of the sensors. F.B. and A.G. wrote the paper with the help of all the authors. All authors have given approval to the final version of the manuscript.

Funding Sources

This work has been supported by the European Research Council (ERC-2016-CoG-724705 FLUOSWITCH) and the French National Research Agency (ANR-21-CE42-0019-02 AmpliSens).

REFERENCES

- (1) Nakai, J.; Ohkura, M.; Imoto, K. A High Signal-to-Noise Ca²⁺ Probe Composed of a Single Green Fluorescent Protein. *Nat Biotechnol* **2001**, *19* (2), 137–141. <https://doi.org/10.1038/84397>.
- (2) Chen, T.-W.; Wardill, T. J.; Sun, Y.; Pulver, S. R.; Renninger, S. L.; Baohan, A.; Schreiter, E. R.; Kerr, R. a; Orger, M. B.; Jayaraman, V.; Looger, L. L.; Svoboda, K.; Kim, D. S. Ultrasensitive Fluorescent Proteins for Imaging Neuronal Activity. *Nature* **2013**, *499* (7458), 295–300. <https://doi.org/10.1038/nature12354>.
- (3) Yang, Y.; Liu, N.; He, Y.; Liu, Y.; Ge, L.; Zou, L.; Song, S.; Xiong, W.; Liu, X. Improved Calcium Sensor GCaMP-X Overcomes the Calcium Channel Perturbations Induced by the Calmodulin in GCaMP. *Nat Commun* **2018**, *9* (1), 1504. <https://doi.org/10.1038/s41467-018-03719-6>.
- (4) Tsien, R. Y. Building and Breeding Molecules to Spy on Cells and Tumors. *FEBS Lett* **2005**, *579* (4 SPEC. ISS.), 927–932. <https://doi.org/10.1016/j.febslet.2004.11.025>.
- (5) Hires, S. A.; Zhu, Y.; Tsien, R. Y. Optical Measurement of Synaptic Glutamate Spillover and Reuptake by Linker Optimized Glutamate-Sensitive Fluorescent Reporters. *Proceedings of the National Academy of Sciences* **2008**, *105* (11), 4411–4416. <https://doi.org/10.1073/pnas.0712008105>.
- (6) Broch, F.; Gautier, A. Illuminating Cellular Biochemistry: Fluorogenic Chemogenetic Biosensors for Biological Imaging. *Chempluschem* **2020**, *85* (7), 1487–1497. <https://doi.org/10.1002/cplu.202000413>.
- (7) Farrants, H.; Hiblot, J.; Griss, R.; Johnsson, K. Chapter 7 Rational Design and Applications of Semisynthetic Modular Biosensors: SNIFITs and LUCIDs. **2017**, *1596*, 101–117. https://doi.org/10.1007/978-1-4939-6940-1_7.
- (8) Yu, Q.; Xue, L.; Hiblot, J.; Griss, R.; Fabritz, S.; Roux, C.; Binz, P. A.; Haas, D.; Okun, J. G.; Johnsson, K. Semisynthetic Sensor Proteins Enable Metabolic Assays at the Point of Care. *Science* (1979) **2018**, *361* (6407), 1122–1126. <https://doi.org/10.1126/science.aat7992>.
- (9) Hellweg, L.; Edenhofer, A.; Barck, L.; Huppertz, M. C.; Frei, M. S.; Tarnawski, M.; Bergner, A.; Koch, B.; Johnsson, K.; Hiblot, J. A General Method for the Development of Multicolor Biosensors with Large Dynamic Ranges. *Nat Chem Biol* **2023**. <https://doi.org/10.1038/s41589-023-01350-1>.
- (10) Ackerman, D. S.; Vasilev, K. V.; Schmidt, B. F.; Cohen, L. B.; Jarvik, J. W. Tethered Fluorogen Assay to Visualize Membrane Apposition in Living Cells. *Bioconjug Chem* **2017**, *28* (5), 1356–1362. <https://doi.org/10.1021/acs.bioconjchem.7b00047>.
- (11) Carpenter, M. A.; Wang, Y.; Telmer, C. A.; Schmidt, B. F.; Yang, Z.; Bruchez, M. P. Protein Proximity Observed Using Fluorogen Activating Protein and Dye Activated by Proximal Anchoring (FAP-DAPA) System. *ACS Chem Biol* **2020**, *15* (9), 2433–2443. <https://doi.org/10.1021/acscchembio.0c00419>.
- (12) Klima, J. C.; Doyle, L. A.; Lee, J. D.; Rappleye, M.; Gagnon, L. A.; Lee, M. Y.; Barros, E. P.; Vorobieva, A. A.; Dou, J.; Bremner, S.; Quon, J. S.; Chow, C. M.; Carter, L.; Mack, D. L.; Amaro, R. E.; Vaughan, J. C.; Berndt, A.; Stoddard, B. L.; Baker, D. Incorporation of Sensing Modalities into de Novo Designed Fluorescence-Activating Proteins. *Nat Commun* **2021**, *12* (1), 1–19. <https://doi.org/10.1038/s41467-020-18911-w>.
- (13) Deo, C.; Abdelfattah, A. S.; Bhargava, H. K.; Berro, A. J.; Falco, N.; Farrants, H.; Moeyaert, B.; Chupanova, M.; Lavis, L. D.; Schreiter, E. R. The HaloTag as a General Scaffold for Far-Red Tunable Chemigenetic Indicators. *Nat Chem Biol* **2021**, *17* (6), 718–723. <https://doi.org/10.1038/s41589-021-00775-w>.
- (14) Stein, V.; Alexandrov, K. Synthetic Protein Switches: Design Principles and Applications. *Trends Biotechnol* **2015**, *33* (2), 101–110. <https://doi.org/10.1016/j.tibtech.2014.11.010>.
- (15) Adamson, H.; Jeuken, L. J. C. Engineering Protein Switches for Rapid Diagnostic Tests. *ACS Sens* **2020**, *5* (10), 3001–3012. <https://doi.org/10.1021/acssensors.0c01831>.
- (16) Zhang, L.; Lee, K. C.; Bhojani, M. S.; Khan, A. P.; Shilman, A.; Holland, E. C.; Ross, B. D.; Rehemtulla, A. Molecular Imaging of Akt Kinase Activity. *Nat Med* **2007**, *13* (9), 1114–1119. <https://doi.org/10.1038/nm1608>.
- (17) Farrants, H.; Tarnawski, M.; Müller, T. G.; Otsuka, S.; Hiblot, J.; Koch, B.; Kueblbeck, M.; Kräusslich, H. G.; Ellenberg, J.; Johnsson, K. Chemogenetic Control of Nanobodies. *Nat Methods* **2020**, *17* (3), 279–282. <https://doi.org/10.1038/s41592-020-0746-7>.
- (18) Plamont, M.-A.; Billon-denis, E.; Maurin, S.; Gauron, C.; Pimenta, F. M.; Specht, C. G.; Shi, J.; Pan, B.; Rossignol, J.; Morellet, N.; Lescop, E.; Chen, Y.; Triller, A.; Saux, T. Le; Jullien, L.; Gautier, A. Small Fluorescence-Activating and Absorption-Shifting Tag for Tunable Protein Imaging in Vivo. *Proceedings of the National Academy of Sciences* **2016**, *113* (10), 497–502. <https://doi.org/10.1073/pnas.1602162113>.
- (19) Li, C.; Plamont, M. A.; Sladitschek, H. L.; Rodrigues, V.; Aujard, I.; Neveu, P.; Le Saux, T.; Jullien, L.; Gautier, A. Dynamic Multicolor Protein Labeling in Living Cells. *Chem Sci* **2017**, *8* (8), 5598–5605. <https://doi.org/10.1039/c7sc01364g>.
- (20) Li, C.; Tebo, A. G.; Thauvin, M.; Plamont, M.; Volovitch, M.; Morin, X.; Vriza, S.; Gautier, A. A Far-Red Emitting Fluorescent Chemogenetic Reporter for In Vivo Molecular Imaging. *Angewandte Chemie* **2020**, *132* (41), 18073–18079. <https://doi.org/10.1002/ange.202006576>.
- (21) Chekli, Y.; Peron-Cane, C.; Dell’Arciprete, D.; Allemand, J. F.; Li, C.; Ghigo, J. M.; Gautier, A.; Lebreton, A.; Desprat, N.; Beloin, C. Visualizing the Dynamics of Exported Bacterial Proteins with the Chemogenetic Fluorescent Reporter FAST. *Sci Rep* **2020**, *10* (1), 1–14. <https://doi.org/10.1038/s41598-020-72498-2>.
- (22) Peron-Cane, C.; José-Carlos Fernandez; Leblanc, J.; Wingertsmann, L.; Gautier, A.; Desprat, N.; Lebreton, A. Fluorescent Secreted Bacterial Effectors Reveal Active Intravascular Proliferation of *Listeria monocytogenes* in Epithelial Cells. *PLoS Pathog* **2020**, *16* (10), 1–29. <https://doi.org/10.1371/journal.ppat.1009001>.
- (23) Tebo, A. G.; Moeyaert, B.; Thauvin, M.; Carlon-Andres, I.; Böken, D.; Volovitch, M.; Padilla-Parra, S.; Dedecker, P.; Vriza, S.; Gautier, A. Orthogonal Fluorescent Chemogenetic Reporters for Multicolor Imaging. *Nat Chem Biol* **2021**, *17* (1), 30–38. <https://doi.org/10.1038/s41589-020-0611-0>.
- (24) Lu, Z.; Peng, B.; Ebert, B. E.; Dumsday, G.; Vickers, C. E. Auxin-Mediated Protein Depletion for Metabolic Engineering in Terpene-Producing Yeast. *Nat Commun* **2021**, *12* (1). <https://doi.org/10.1038/s41467-021-21313-1>.
- (25) Benaissa, H.; Ounoughi, K.; Aujard, I.; Fischer, E.; Goïame, R.; Nguyen, J.; Tebo, A. G.; Li, C.; Saux, T. Le; Danglot, L.; Pietrancosta, N.; Morin, X.; Jullien, L.; Gautier, A. Engineering of a Fluorescent Chemogenetic Reporter with Tunable Color for Advanced Live-Cell Imaging. *Nat Commun* **2021**, *12*, 2021.01.29.428635. <https://doi.org/10.1038/s41467-021-27334-0>.
- (26) Monmeyran, A.; Thomen, P.; Jonquière, H.; Sureau, F.; Li, C.; Plamont, M. A.; Douarce, C.; Casella, J. F.; Gautier, A.; Henry, N. The Inducible Chemical-Genetic Fluorescent Marker FAST Outperforms Classical Fluorescent Proteins in the Quantitative Reporting of Bacterial Biofilm Dynamics. *Sci Rep* **2018**, *8* (1), 10336. <https://doi.org/10.1038/s41598-018-28643-z>.

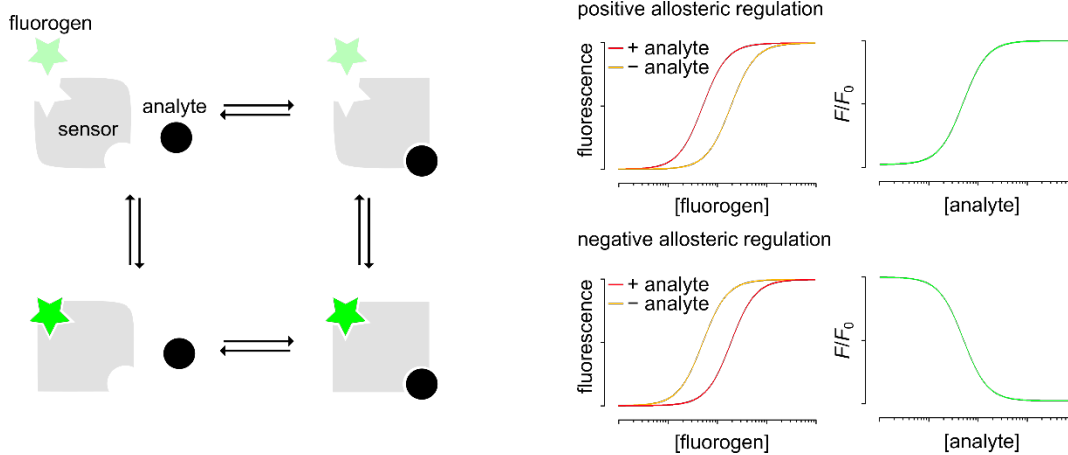
- (27) Streett, H. E.; Kalis, K. M.; Papoutsakis, E. T. A Strongly Fluorescing Anaerobic Reporter and Protein-Tagging System for Clostridium Organisms Based on FAST. *Appl Environ Microbiol* **2019**, *85* (14), e00622-19.
- (28) Charubin, K.; Streett, H.; Papoutsakis, E. T. Development of Strong Anaerobic Fluorescent Reporters for Clostridium Acetobutylicum and Clostridium Ljungdahlii Using HaloTag and SNAP-Tag Proteins. *Appl Environ Microbiol* **2020**, *86* (20), e01271-20.
- (29) Charubin, K.; Modla, S.; Caplan, J. L.; Papoutsakis, E. T. Interspecies Microbial Fusion and Large-Scale Exchange of Cytoplasmic Proteins and RNA in a Syntrophic Clostridium Coculture. *mBio* **2020**, *11* (5), e02030-20.
- (30) Flaiz, M.; Ludwig, G.; Bengelsdorf, F. R.; Dürre, P. Production of the Biocommodities Butanol and Acetone from Methanol with Fluorescent FAST-Tagged Proteins Using Metabolically Engineered Strains of Eubacterium Limosum. *Biotechnol Biofuels* **2021**, *14* (1), 1-20. <https://doi.org/10.1186/s13068-021-01966-2>.
- (31) Tebo, A. G.; Pimenta, F. M.; Zoumpoulaki, M.; Kikuti, C.; Sirkia, H.; Plamont, M.-A.; Houdusse, A.; Gautier, A. Circularly Permuted Fluorogenic Proteins for the Design of Modular Biosensors. *ACS Chem Biol* **2018**, *13* (9), 2392-2397. <https://doi.org/10.1021/acscchembio.8b00417>.
- (32) Tebo, A. G.; Gautier, A. A Split Fluorescent Reporter with Rapid and Reversible Complementation. *Nat Commun* **2019**, *10* (1), 2822. <https://doi.org/10.1038/s41467-019-10855-0>.
- (33) Bottone, S.; Joliot, O.; Cakil, Z. V.; El Hajji, L.; Rakotoarison, L.-M.; Boncompain, G.; Perez, F.; Gautier, A. A Fluorogenic Chemically Induced Dimerization Technology for Controlling, Imaging and Sensing Protein Proximity. *Nat Methods* **2023**. <https://doi.org/10.1038/s41592-023-01988-8>.
- (34) Platt, S. R. The Role of Glutamate in Central Nervous System Health and Disease - A Review. *Veterinary Journal* **2007**, *173* (2), 278-286. <https://doi.org/10.1016/j.tvjl.2005.11.007>.
- (35) Nedergaard, M.; Takano, T.; Hansen, A. J. Beyond the Role of Glutamate as a Neurotransmitter. *Nat Rev Neurosci* **2002**, *3* (9), 748-755. <https://doi.org/10.1038/nrn916>.
- (36) Okumoto, S.; Looger, L. L.; Micheva, K. D.; Reimer, R. J.; Smith, S. J.; Frommer, W. B. Detection of Glutamate Release from Neurons by Genetically Encoded Surface-Displayed FRET Nanosensors. *Proceedings of the National Academy of Sciences* **2005**, *102* (24), 8740-8745. <https://doi.org/10.1073/pnas.0503274102>.
- (37) Marvin, J. S.; Borghuis, B. G.; Tian, L.; Cichon, J.; Harnett, M. T.; Akerboom, J.; Gordus, A.; Renninger, S. L.; Chen, T. W.; Bargmann, C. I.; Orger, M. B.; Schreiter, E. R.; Demb, J. B.; Gan, W. B.; Hires, S. A.; Looger, L. L. An Optimized Fluorescent Probe for Visualizing Glutamate Neurotransmission. *Nat Methods* **2013**, *10* (2), 162-170. <https://doi.org/10.1038/nmeth.2333>.
- (38) Wu, J.; Abdelfattah, A. S.; Zhou, H.; Ruangkittisakul, A.; Qian, Y.; Ballanyi, K.; Campbell, R. E. Genetically Encoded Glutamate Indicators with Altered Color and Topology. *ACS Chem Biol* **2018**, *acschembio.7b01085*. <https://doi.org/10.1021/acscchembio.7b01085>.
- (39) Ashraf, K. U.; Josts, I.; Mosbahi, K.; Kelly, S. M.; Byron, O.; Smith, B. O.; Walker, D. The Potassium Binding Protein Kbp Is a Cytoplasmic Potassium Sensor. *Structure* **2016**, *24* (5), 741-749. <https://doi.org/10.1016/j.str.2016.03.017>.
- (40) Bischof, H.; Rehberg, M.; Stryeck, S.; Artinger, K.; Eroglu, E.; Waldeck-Weiermair, M.; Gottschalk, B.; Rost, R.; Deak, A. T.; Niedrist, T.; Vujic, N.; Lindermuth, H.; Prassl, R.; Pelzmann, B.; Groschner, K.; Kratky, D.; Eller, K.; Rosenkranz, A. R.; Madl, T.; Plesnila, N.; Graier, W. F.; Malli, R. Novel Genetically Encoded Fluorescent Probes Enable Real-Time Detection of Potassium in Vitro and in Vivo. *Nat Commun* **2017**, *8* (1), 1-11. <https://doi.org/10.1038/s41467-017-01615-z>.
- (41) Shen, Y.; Wu, S.-Y.; Rancic, V.; Aggarwal, A.; Qian, Y.; Miyashita, S.-I.; Ballanyi, K.; Campbell, R. E.; Dong, M. Genetically Encoded Fluorescent Indicators for Imaging Intracellular Potassium Ion Concentration. *Commun Biol* **2019**, *2* (1), 18. <https://doi.org/10.1038/s42003-018-0269-2>.
- (42) Palmer, B. F. Regulation Of Potassium Homeostasis. *Clinical Journal of the American Society of Nephrology* **2014**, *10* (6), 1050-1060. <https://doi.org/10.2215/CJN.08580813>.
- (43) Kato, S.; Yoshida, M.; Kato-Yamada, Y. Role of the ϵ Subunit of Thermophilic F1-ATPase as a Sensor for ATP. *Journal of Biological Chemistry* **2007**, *282* (52), 37618-37623. <https://doi.org/10.1074/jbc.M707509200>.
- (44) Yagi, H.; Kajiwara, N.; Tanaka, H.; Tsukihara, T.; Kato-Yamada, Y.; Yoshida, M.; Akutsu, H. Structures of the Thermophilic F1-ATPase ϵ Subunit Suggesting ATP-Regulated Arm Motion of Its C-Terminal Domain in F1. *Proc Natl Acad Sci U S A* **2007**, *104* (27), 11233-11238. <https://doi.org/10.1073/pnas.0701045104>.
- (45) Imamura, H.; Huynh Nhat, K. P.; Togawa, H.; Saito, K.; Iino, R.; Kato-Yamada, Y.; Nagai, T.; Noji, H. Visualization of ATP Levels inside Single Living Cells with Fluorescence Resonance Energy Transfer-Based Genetically Encoded Indicators. *Proc Natl Acad Sci U S A* **2009**, *106* (37), 15651-15656. <https://doi.org/10.1073/pnas.0904764106>.
- (46) Lobas, M. A.; Tao, R.; Nagai, J.; Kronschläger, M. T.; Borden, P. M.; Marvin, J. S.; Looger, L. L.; Khakh, B. S. A Genetically Encoded Single-Wavelength Sensor for Imaging Cytosolic and Cell Surface ATP. *Nat Commun* **2019**, *10* (1). <https://doi.org/10.1038/s41467-019-08441-5>.
- (47) Kitajima, N.; Takikawa, K.; Sekiya, H.; Satoh, K.; Asanuma, D.; Sakamoto, H.; Takahashi, S.; Hanaoka, K.; Urano, Y.; Namiki, S.; Iino, M.; Hirose, K. Real-Time in Vivo Imaging of Extracellular Atp in the Brain with a Hybrid-Type Fluorescent Sensor. *Elife* **2020**, *9*, 1-18. <https://doi.org/10.7554/eLife.57544>.
- (48) Yaginuma, H.; Kawai, S.; Tabata, K. V.; Tomiyama, K.; Kakizuka, A.; Komatsuzaki, T.; Noji, H.; Imamura, H. Diversity in ATP Concentrations in a Single Bacterial Cell Population Revealed by Quantitative Single-Cell Imaging. *Sci Rep* **2014**, *4*. <https://doi.org/10.1038/srep06522>.
- (49) Monod, J.; Wyman, J.; Changeux, J. P. On the Nature of Allosteric Transitions: A Plausible Model. *J Mol Biol* **1965**, *12* (1), 88-118. [https://doi.org/10.1016/S0022-2836\(65\)80285-6](https://doi.org/10.1016/S0022-2836(65)80285-6).
- (50) Giardina, B.; Ascenzi, P.; Clementi, M. E.; De Sanctis, G.; Rizzi, M.; Coletta, M. Functional Modulation by Lactate of Myoglobin. A Monomeric Allosteric Hemoprotein. *Journal of Biological Chemistry* **1996**, *271* (29), 16999-17001. <https://doi.org/10.1074/jbc.271.29.16999>.
- (51) Volkman, B. F.; Lipson, D.; Wemmer, D. E.; Kern, D. Two-State Allosteric Behavior in a Single-Domain Signaling Protein. *Science* (1979) **2001**, *291* (5512), 2429-2433. <https://doi.org/10.1126/science.291.5512.2429>.
- (52) Velazquez-Campoy, A.; Goñi, G.; Peregrina, J. R.; Medina, M. Exact Analysis of Heterotropic Interactions in Proteins: Characterization of Cooperative Ligand Binding by Isothermal Titration Calorimetry. *Biophys J* **2006**, *91* (5), 1887-1904. <https://doi.org/10.1529/biophysj.106.086561>.
- (53) Shitashima, Y.; Shimozaawa, T.; Asahi, T.; Miyawaki, A. A Dual-Ligand-Modulable Fluorescent Protein Based on UnaG and Calmodulin. *Biochem Biophys Res Commun* **2018**, *496* (3), 872-879. <https://doi.org/10.1016/j.bbrc.2018.01.134>.
- (54) Jumper, J.; Evans, R.; Pritzel, A.; Green, T.; Figurnov, M.; Ronneberger, O.; Tunyasuvunakool, K.; Bates, R.; Židek, A.; Potapenko, A.; Bridgland, A.; Meyer, C.; Kohl, S. A. A.; Ballard, J. J.; Cowie, A.; Romera-Paredes, B.; Nikolov, S.; Jain, R.; Adler, J.; Back, T.; Petersen, S.; Reiman, D.; Clancy, E.; Zielinski, M.; Steinegger, M.; Pacholska, M.; Berghammer, T.; Bodenstein, S.; Silver, D.; Vinyals, O.; Senior, A. W.; Kavukcuoglu, K.; Kohli, P.; Hassabis,

D. Highly Accurate Protein Structure Prediction with AlphaFold.
Nature **2021**, *596* (7873), 583–589.
<https://doi.org/10.1038/s41586-021-03819-2>.
(55) Gibson, D. G.; Young, L.; Chuang, R.-Y.; Venter, J. C.;
Hutchison, C. a; Smith, H. O.; Iii, C. A. H.; America, N. Enzymatic
Assembly of DNA Molecules up to Several Hundred Kilobases.

Nat Methods **2009**, *6* (5), 343–345.
<https://doi.org/10.1038/nmeth.1318>.

SYNOPSIS TOC

Here, we applied the concept of allosteric regulation to construct fluorescent protein-based switches responsive to specific analytes. Incorporation of sensing units into the chemogenetic fluorescence-activating and absorption-shifting tag (FAST) that reversibly binds and stabilizes the fluorescent state of 4-hydroxybenzylidene rhodanine (HBR) derivatives allowed us to generate fluorescent sensors responding to biological analytes. We show that conformational coupling between FAST and the sensing domain can generate allosteric-like behavior, in which fluorogen binding, and therefore fluorescence, is conditioned to analyte recognition.



For TOC only

Supplementary Information

Engineering of Tunable Allosteric-Like Fluorogenic Protein Sensors

Fanny Broch,^[a] Lina El Hajji,^[a] Nicolas Pietrancosta^[a,b] & Arnaud Gautier^{*,[a,c]}

^[a] Sorbonne Université, École Normale Supérieure, Université PSL, CNRS, Laboratoire des Biomolécules, LBM, 75005 Paris, France

^[b] Neurosciences Paris Seine-Institut de Biologie Paris Seine (NPS-IBPS) INSERM, CNRS, Sorbonne Université, Paris, France

^[c] Institut Universitaire de France

* Correspondence should be sent to: arnaud.gautier@sorbonne-universite.fr

This PDF file includes

Methods

Supplementary Text S1

Supplementary Figures S1-S15

Supplementary Tables S1-S8

Supplementary References

Methods

General Synthetic oligonucleotides used for cloning were purchased from Integrated DNA Technology. PCR reactions were performed with Q5 polymerase (New England Biolabs) in the buffer provided. PCR products were purified using QIAquick PCR purification kit (Qiagen). Isothermal assemblies (Gibson assembly) were performed using homemade mix prepared according to previously described protocols (modified from the original described protocol).¹ Gibson products were purified using MinElute PCR purification kit (Qiagen). Gibson products were transformed in DH10 E. coli. Small-scale isolation of plasmid DNA was done using QIAprep miniprep kit (Qiagen) from 3 mL of overnight culture supplemented with appropriate antibiotics. Large-scale isolation of plasmid DNA was done using the QIAprep maxiprep kit (Qiagen) from 150 mL of overnight culture supplemented with appropriate antibiotics. All plasmid sequences were confirmed by Sanger sequencing with appropriate sequencing primers (GATC Biotech). The preparation of HMBR, HBR-3,5DOM and HBR-3,5DM was previously described.^{2,3}

Protein expression and purification Expression vectors of the glutamate and ATP biosensors with an N-terminal His-tag under the control of a T7 promoter were transformed in Rosetta(DE3)pLysS Escherichia coli competent cells. Bacterial cells were grown at 37 °C in Lysogeny Broth (LB) supplemented with chloramphenicol (34 µg/mL) and kanamycin (50 µg/mL) until $OD_{600nm} = 0.6$. Expression vectors of the K⁺ biosensors with an N-terminal His-tag under the control of a T7 promoter were transformed in BL21 Escherichia coli competent cells. Bacterial cells were grown at 37 °C in Lysogeny Broth (LB) supplemented with kanamycin (50 µg/mL) until $OD_{600nm} = 0.6$. Expression was induced overnight at 16°C by the addition of isopropyl β-D-1-thiogalactopyranoside (IPTG) (1 mM). Cells were harvested by centrifugation (4000 × g for 20 min at 4°C) and stored at -30°C. The cell pellets were resuspended in lysis buffer (TES 1×: trisaminomethane (Tris) 200 mM, EDTA 0.65 mM and sucrose 0.5 M, protease inhibitor PMSF 1 mM, DNase 0.025 mg/mL, MgCl₂ 5 mM) and kept on ice for 1h, followed by resuspension in TES 0.25 × to induce lysis by osmotic choc. Cellular fragments were removed by centrifugation (9200 × g for 1h at 4°C). The supernatant was incubated overnight at 4°C by gentle agitation with Ni-NTA agarose beads in Tris (50 mM), NaCl (150 mM) buffer with 20 mM imidazole. The beads were then washed sequentially with 10 volumes of Tris (50 mM), NaCl (150 mM) buffer with 20 mM imidazole, then with 5 volumes of Tris buffer complemented with 40mM imidazole, and the proteins were eluted with 3 volumes of Tris buffer with 0.5 M imidazole. The buffer was afterwards exchanged with HEPES buffer (HEPES 50 mM, NaCl 150 mM pH 8 for glutamate sensors, HEPES 50mM, MgCl₂ 75 mM pH 8 for K⁺ and ATP sensors) using PD-10 or PD-MidiTrap G-25 desalting columns (GE Healthcare). Purity of the proteins was evaluated using SDS-PAGE electrophoresis stained with Coomassie blue.

Thermodynamic analysis Determination of the thermodynamic constants by titration experiments were performed with a Spark 10M plate reader (Tecan) in HEPES buffer (HEPES 50 mM, NaCl 150 mM pH 7.4 for glutamate sensors, HEPES 50mM, MgCl₂ 75 mM pH 7.4 for K⁺ and ATP sensors). Normalized fluorescence intensity was plotted as a function of fluorogen concentration and fitted in GraphPad Prism 7 to a one-site specific binding model.

Determination of glucose concentrations Glucose samples were prepared in HEPES buffer (50 mM) containing MgCl₂ (75 mM) and were either evaluated with the Glucose (HK) Assay Kit (Sigma-Aldrich) or with our home-made assay containing 1 unit of enzyme mix HK-G6P (Sigma-Aldrich), 0.1 µM purified sensor mCherry-ATP-FAST-1 and 1 µM HMBR in HEPES buffer (50 mM) containing MgCl₂ (75 mM). After a 30min incubation at 25°C, absorbance was measured with a biophotometer (Eppendorf) and fluorescence was measured Spark 10M plate reader (Tecan).

Modeling Molecular modeling are performed using similar protocol than we previously described (12). Briefly, homology model of sensors are generated based on PYP and appropriated GLU/K+/ATP binding proteins (respectively pdb code: 2vha; 7pvc; 6fgf; 5e5y). Alignments were manually refined to avoid gaps in predicted and known secondary structure elements. Three-dimensional FAST sensor models were built from these alignments and from crystallographic atomic coordinates of template using the automated comparative modeling tool MODELER (Sali and Blundell) implemented in Discovery Studio. The best model according to DOPE score (Discrete Optimized Protein Energy) and potential energy calculated by modeler were solvated (10 Å water box and 0.145 M NaCl) and minimized using Adopted Basis NR algorithm to a final gradient of 0.001. The resulting structure were submitted to a 30 ns NAMD dynamics (for Glutamate and Potassium sensors) and 2 ns NAMD dynamics for the ATP sensor. Molecular docking was also performed using previously described protocols (12). Briefly, flexible ligand-rigid protein docking was performed using CDOCKER implemented in Discovery Studio. Random ligand conformations were generated from the initial ligand structure through high-temperature molecular dynamics. The best poses according to their ligscore were retained and clustered according to their binding mode. The most significant poses were solvated and minimized using Adopted Basis NR algorithm to a final gradient of 0.001.

Molecular cloning Designations NFAST and CFAST stand for FAST(1-114) and FAST(115-125), respectively, and N-pFAST and C-pFAST stand for pFAST(1-114) and pFAST(115-125).

The plasmid pAG399, encoding His-FAST, was constructed by Gibson assembly from the plasmid pAG104 encoding CMV-FAST². The synthetic pET28 backbone was amplified by PCR using the primers ag578/kanR and ag579/kanF. The insert was amplified by PCR using the primers ag601/ag602. The three fragments were then assembled by Gibson assembly.

The plasmid pAG400 encoding His-cpFAST2, was constructed by Gibson assembly from the plasmid pAG120 encoding His-tev-FAST.⁴ The synthetic pET28 backbone was amplified by PCR using the primers ag578/kanR and ag579/kanF. The insert was amplified by PCR using the primers ag603/ag604. The three fragments were then assembled by Gibson assembly.

The plasmid pAG401 encoding His-Kbp, was constructed by Gibson assembly from a synthetic gene. The synthetic pET28 backbone was amplified by PCR using the primers ag578/kanR and ag579/kanF. The insert was amplified by PCR using the primers ag605/ag606. The three fragments were then assembled by Gibson assembly.

The plasmid pAG402 encoding His-GltI was constructed by Gibson assembly from a synthetic gene. The synthetic pET28 backbone was amplified by PCR using the primers ag578/kanR and ag579/kanF. The insert was amplified by PCR using the primers ag601/ag602. The three fragments were then assembled by Gibson assembly.

The plasmid pAG403 encoding His-cpGltI was constructed by Gibson assembly from a synthetic gene. The synthetic pET28 backbone was amplified by PCR using the primers ag578/kanR and ag579/kanF. The inserts NGltI and CGltI were amplified by PCR using the primers ag609/ag610 and ag611/ag612. The four fragments were then assembled by Gibson assembly.

The plasmid pAG729 encoding His-B.PS3 was constructed by Gibson assembly from a synthetic gene. The synthetic pET28 backbone was amplified by PCR using the primers ag578/kanR and ag579/kanF. The insert was amplified by PCR using the primers ag1033/ag1034. The three fragments were then assembled by Gibson assembly.

The plasmid pAG445, encoding His-Glu-FAST-1, was constructed by Gibson assembly from the plasmid pAG399 encoding His-FAST. The fragment coding for NFAST was amplified by PCR using the primers ag630/kanF. The fragment coding for CFAST was amplified using the primers ag629/kanR. The insert coding for GltI was amplified from pAG402 encoding His-GltI using the primers ag631/ag632. The three fragments were then assembled by Gibson assembly.

The plasmid pAG446, encoding His-cpGlu-FAST-1, was constructed by Gibson assembly from the plasmid pAG403 encoding His-cpGltI. The fragment coding for CGltI was amplified by PCR using the primers ag632/kanF. The fragment coding for NGltI was amplified using the primers ag631/kanR. The insert coding for cpFAST2 was amplified from pAG400 encoding cpFAST2 using the primers ag629/ag630. The three fragments were then assembled by Gibson assembly.

The plasmid pAG447, encoding His-Glu-FAST-2, was constructed by Gibson assembly from the plasmid pAG400 encoding cpFAST2. The fragment coding for CFAST was amplified by PCR using the primers ag634/kanF. The fragment coding for NFAST was amplified using the primers ag633/kanR. The insert coding for GltI was amplified from pAG402 encoding His-GltI using the primers ag635/ag636. The three fragments were then assembled by Gibson assembly.

The plasmid pAG448, encoding His-cpGlu-FAST-2, was constructed by Gibson assembly from the plasmid pAG403 encoding His-cpGltI. The fragment coding for CGltI was amplified by PCR using the primers ag636/kanF. The fragment coding for NGltI was amplified using the primers ag635/kanR. The insert coding for FAST was amplified from pAG399 encoding His-FAST using the primers ag633/ag634. The three fragments were then assembled by Gibson assembly.

The plasmid pAG449, encoding His-Glu-FAST-3, was constructed by Gibson assembly from the plasmid pAG402 encoding His-GltI. The fragment coding for NGltI was amplified by PCR in two fragments, using the primers ag607/ag638 and ag579/kanF. The fragment coding for CGltI was amplified using the primers ag637/kanR. The insert coding for FAST was amplified from pAG399 encoding His-FAST using the primers ag639/ag640. The four fragments were then assembled by Gibson assembly.

The plasmid pAG450, encoding His-cpGlu-FAST-3, was constructed by Gibson assembly from the plasmid pAG400 encoding His-cpFAST2. The fragment coding for CFAST was amplified by PCR using the primers ag640/kanF. The fragment coding for NFAST was amplified using the primers ag639/kanR. The insert coding for cpGltI was amplified from pAG403 encoding His-cpGltI using the primers ag637/ag638. The three fragments were then assembled by Gibson assembly.

The plasmid pAG451, encoding His-Glu-FAST-4, was constructed by Gibson assembly from the plasmid pAG402 encoding His-GltI. The fragment coding for NGltI was amplified by PCR in two fragments, using the primers ag607/ag642 and ag579/kanF. The fragment coding for CGltI was amplified using the primers ag641/kanR. The insert coding for cpFAST2 was amplified from pAG400 encoding His-cpFAST2 using the primers ag643/ag644. The four fragments were then assembled by Gibson assembly.

The plasmid pAG452, encoding His-cpGlu-FAST-4, was constructed by Gibson assembly from the plasmid pAG399 encoding His-FAST. The fragment coding for NFAST was amplified by PCR using the primers ag644/kanF. The fragment coding for CFAST was amplified using the primers ag643/kanR. The insert coding for cpGltI was amplified from pAG403 encoding His-cpGltI using the primers ag641/ag642. The three fragments were then assembled by Gibson assembly.

The plasmid pAG513, encoding His-Glu-FAST-2-CFAST(116-125), was constructed by Gibson assembly from the plasmid pAG447. The pET28 backbone was amplified by PCR using the primers ag579/kanF. The fragment coding for CFAST(116-125)-GltI-NFAST was amplified using the primers ag804/kanR. The two fragments were then assembled by Gibson assembly.

The plasmid pAG634, encoding His-Glu-FAST-2-CFAST10-PP(2) (His-Glu-FAST-2.1), was constructed by Gibson assembly from the plasmids pAG513. The fragment coding for CFAST(116-125)-GltI was amplified by PCR using the primers ag910/kanF. The fragment coding for NFAST was amplified using the primers ag704/kanR. The two fragments were then assembled by Gibson assembly.

The plasmid pAG441, encoding His-K⁺-FAST-1, was constructed by Gibson assembly from the plasmid pAG399 encoding His-FAST. The fragment coding for NFAST was amplified by PCR using the primers ag614/kanF. The fragment coding for CFAST was amplified using the primers ag613/kanR. The insert coding for Kbp was amplified from pAG401 encoding His-Kbp using the primers ag615/ag616. The three fragments were then assembled by Gibson assembly.

The plasmid pAG442, encoding His-K⁺-FAST-2, was constructed by Gibson assembly from the plasmid pAG400 encoding His-cpFAST2. The fragment coding for CFAST was amplified by PCR using the primers ag618/kanF. The fragment coding for NFAST was amplified using the primers ag617/kanR. The insert coding for Kbp was amplified from pAG401 encoding His-Kbp using the primers ag619/ag620. The three fragments were then assembled by Gibson assembly.

The plasmid pAG443, encoding His-K⁺-FAST-3, was constructed by Gibson assembly from the plasmid pAG401 encoding His-Kbp. The fragment coding for BON was amplified by PCR using the primers ag622/kanF. The fragment coding for Lys was amplified using the primers ag621/kanR. The insert coding for FAST was amplified from pAG399 encoding His-FAST using the primers ag623/ag624. The three fragments were then assembled by Gibson assembly.

The plasmid pAG444, encoding His-K⁺-FAST-4, was constructed by Gibson assembly from the plasmid pAG401 encoding His-Kbp. The fragment coding for BON was amplified by PCR using the primers ag626/kanF. The fragment coding for Lys was amplified using the primers ag625/kanR. The insert coding for cpFAST2 was amplified from pAG400 encoding His-cpFAST2 using the primers ag627/ag628. The three fragments were then assembled by Gibson assembly.

The plasmid pAG512, encoding His-K⁺-FAST-5, was constructed by Gibson assembly from the plasmid pAG442. The fragment coding for CFAST-GG-BON was amplified by PCR using the primer ag732 containing the sequence coding for linker (GGGGS)₃, with the primer kanF. The fragment coding for Lys-GG-NFAST was amplified using the primer ag731 containing the complementary sequence coding for linker (GGGGS)₃, with the primer kanR. The two fragments were then assembled by Gibson assembly.

The plasmid pAG625, encoding His-K⁺-FAST-5.1, was constructed by Gibson assembly from the plasmid pAG512. The pET28 backbone was amplified by PCR using the primers ag579/kanF. The insert coding for CFAST(116-125)-GG-Kbp(GGGGS)₃-GG-NFAST was amplified by PCR using the primers ag804/kanR. The two fragments were then assembled by Gibson assembly.

The plasmid pAG733, encoding ATP-FAST-1, was constructed by Gibson assembly from the plasmid pAG399 encoding His-FAST. The fragment coding for NFAST was amplified by PCR using the primers ag1049/kanF. The fragment coding for CFAST was amplified using the primers ag1048/kanR. The insert coding for *B.PS3* ε was amplified by PCR from the plasmid pAG729 using the primers ag1046/ag1047. The three fragments were then assembled by Gibson assembly.

The plasmid pAG734, encoding ATP-FAST-2, was constructed by Gibson assembly from the plasmid pAG400 encoding His-cpFAST. The fragment coding for CFAST was amplified by PCR using the primers ag1050/kanF. The fragment coding for NFAST was amplified using the primers ag1051/kanR. The insert coding for the *B.PS3* ε was amplified by PCR from the plasmid pAG729 using the primers ag1046/ag1047. The three fragments were then assembled by Gibson assembly.

The plasmid pAG735 and pAG736, encoding the ATP-FAST-3 and ATP-FAST-4, respectively, were constructed by Gibson assembly from the plasmid pAG729 encoding *B.PS3* ε. The fragment coding for N-*B.PS3* ε was amplified by PCR using the primers ag1058/kanF. The fragment coding for NFAST was amplified using the primers ag1052/kanR. The insert coding for FAST or cpFAST were amplified by PCR from the plasmid pAG399 or pAG400, respectively, using the primers ag1059/ag1060 or ag1061/1062, respectively. The three fragments were then assembled by Gibson assembly.

The plasmid pAG881, encoding ATP-pFAST-1, was constructed by Gibson assembly from the plasmid pAG641 encoding His-pFAST.⁴ The fragment coding for the pET28 backbone was amplified by PCR using the primers ag579/kanF. The fragment coding for C-pFAST was amplified by PCR using the primers ag1259/kanR. The insert coding for N-pFAST was amplified using the primers ag601/1260. The insert coding for *B.PS3* ε was amplified by PCR from the plasmid pAG729 using the primers ag1046/ag1047. The four fragments were then assembled by Gibson assembly.

The plasmids pAG1008 and pAG1021, encoding mCherry-ATP-pFAST-1 and mCherry-ATP-FAST-1 respectively, were constructed by Gibson assembly from the plasmids pAG881 and pAG733. The fragment coding for mCherry was amplified by PCR using primers ag1566/kanF. The fragments coding for ATP-pFAST-1 and ATP-FAST-1 were amplified by PCR using the primers ag336/kanR. The two fragments were then assembled by Gibson assembly.

The plasmids pAG1091 and pAG1092, encoding ATP-FAST-1-R112K/R126K and ATP-pFAST-1-R122K/R126K respectively, were constructed by Gibson assembly from the plasmids pAG733 and pAG881. The fragment coding for the pET28 backbone was amplified by PCR using the primers ag579/kanF. The fragment coding for CFAST and C-pFAST were amplified by PCR using the primers ag1704/kanR. The inserts coding for NFAST-*B.PS3* ε or N-pFAST-*B.PS3* ε were amplified by PCR using the primers ag601/1703. The three fragments were then assembled by Gibson assembly.

Sequences

Protein sequence of FAST:

EHVAFGSEDIENTLAKMDDGQLDGLAFGAIQLDGDGNILQYNAAEGDITGRDPKQVIGKNF-
FKDVAPGTDSPFYGKFKKEGVASGNLNTMFEWMIPTSRGPTKVKVHMKKALSGDSYWVFKRV

Protein sequence of cpFAST2:

GDSYWVFKRV**GGSE**EHVAFGSEDIENTLAKMDDGQLDGLAFGAIQLDGDGNILQYNAAEG-
DITGRDPKQVIGKNFFKDVAPGTDSPFYGKFKKEGVASGNLNTMFEWMIPTSRGPTKVKVHMKKALS

Protein sequence of Glu-FAST-1:

EHVAFGSEDIENTLAKMDDGQLDGLAFGAIQLDGDGNILQYNAAEGDITGRDPKQVIGKNF-
FKDVAPGTDSPFYGKFKKEGVASGNLNTMFEWMIPTSRGPTKVKVHMKKALS**AAGSTLDKIAKNGVIVVGHRES**

SVPFSYYDNQQKVVGYSDYSNAIVEAVKKKLNKPDQLQVKLIPITSQNRIPLLQNGTFD-
FECGSTTNNVERQKQAAFSDTIFVVGTRLLTKKGGDIKDFANLKDKAVVVTSGTTSEVLLNKLNEEQKMMRIISA
KDHGDSFRTLESGRAVAFMMDDVLLAGERAKAKKPDNWEIV-
GKPQSQEAYGCMLRKDDPQFKKLMDDTIAQVQTSGEAEKWFDKWFKNPIPPKLNLMNFELSDMKALFKEPND
KALKGDSYWVFKRV

Protein sequence of cpGlu-FAST-1:

KLNLMNFELSDMKALFKEPNDKALKGDSYWVFKRV**GGSE**HVAFGSEDIENTLAKMDDGQLDGLAFGAIQLD
GDGNILQYNAAEGDITGRDPKQVIGKNFFKDVAPGTDSPFYGKFKFEGVASGNLNTMFEWMIPTSRGPTKVKVH
MKKALS**AAGSTL**DKIAKNGVIVVGHRESSVPFSYYDNQQKVVGYSDYSNAIVEAVKKKLNKPDQLQVKLIPITSQ
RIPLLQNGTFDFECGSTTNNVERQKQAAFSDTIFVVGTRLLTKKGGDIKDFANLKDKAVVVTSGTTSEVLLNKLNE
EQKMMRIISAKDHGDSFRTLESGRAVAFMMDDVLLAGERAKAKKPDNWEIVGKPQSQEAYGCMLRKDDPQFK
KLMDDTIAQVQTSGEAEKWFDKWFKNPIPP

Protein sequence of Glu-FAST-2:

GDSYWVFKRVA**AAGSTL**DKIAKNGVIVVGHRESSVPFSYYDNQQKVVGYSDYSNAIVEAVKKKLNKPDQLQVKLI
PITSQNRIPLLQNGTFDFECGSTTNNVERQKQAAFSDTIFVVGTRLLTKKGGDIKDFANLKDKAVVVTSGTTSEV
LNKLNEEQKMMRIISAKDHGDSFRTLESGRAVAFMMDDVLLAGERAKAKKPDNWEIVGKPQSQEAYGCMLRK
DDPQFKKLMDDTIAQVQTSGEAEKWFDKWFKNPIPPKLNLMNFELSDMKALFKEPNDKALK**EHVAFGSEDIEN**
TLAKMDDGQLDGLAFGAIQLDGDGNILQYNAAEGDITGRDPKQVIGKNFFKDVAPGTDSPFYGKFKFEGVASGN
LNTMFEWMIPTSRGPTKVKVHMKKALS

Protein sequence of cpGlu-FAST-2:

KLNLMNFELSDMKALFKEPNDKALK**EHVAFGSEDIEN**TLAKMDDGQLDGLAFGAIQLDGDGNILQYNAAEGDIT
GRDPKQVIGKNFFKDVAPGTDSPFYGKFKFEGVASGNLNTMFEWMIPTSRGPTKVKVHMKKALSGDSYWVFK
RVA**AAGSTL**DKIAKNGVIVVGHRESSVPFSYYDNQQKVVGYSDYSNAIVEAVKKKLNKPDQLQVKLIPITSQNRIPLL
QNGTFDFECGSTTNNVERQKQAAFSDTIFVVGTRLLTKKGGDIKDFANLKDKAVVVTSGTTSEVLLNKLNEEQK
MMRIISAKDHGDSFRTLESGRAVAFMMDDVLLAGERAKAKKPDNWEIVGKPQSQEAYGCMLRKDDPQFKKLM
DTIAQVQTSGEAEKWFDKWFKNPIPP

Protein sequence of Glu-FAST-3:

AAGSTLDKIAKNGVIVVGHRESSVPFSYYDNQQKVVGYSDYSNAIVEAVKKKLNKPDQLQVKLIPITSQNRIPLLQ
NGTFDFECGSTTNNVERQKQAAFSDTIFVVGTRLLTKKGGDIKDFANLKDKAVVVTSGTTSEVLLNKLNEEQKMM
RIISAKDHGDSFRTLESGRAVAFMMDDVLLAGERAKAKKPDNWEIVGKPQSQEAYGCMLRKDDPQFKKLMDD
TIAQVQTSGEAEKWFDKWFKN**PILV**EHVAFGSEDIENTLAKMDDGQLDGLAFGAIQLDGDGNILQYNAAEGDITG
RDPKQVIGKNFFKDVAPGTDSPFYGKFKFEGVASGNLNTMFEWMIPTSRGPTKVKVHMKKALSGDSYWVFKR
VNPLNLMNFELSDMKALFKEPNDKALK

Protein sequence of cpGlu-FAST-3:

GDSYWVFKR**VNPLNLMNFELSDMKALFKEPNDKALKGGSHHHHHHGMASMTGGQQMGRDLYDDDDKDPG**
SSGSAAGSTLDKIAKNGVIVVGHRESSVPFSYYDNQQKVVGYSDYSNAIVEAVKKKLNKPDQLQVKLIPITSQNR
IPLLQNGTFDFECGSTTNNVERQKQAAFSDTIFVVGTRLLTKKGGDIKDFANLKDKAVVVTSGTTSEVLLNKLNEE
QKMMRIISAKDHGDSFRTLESGRAVAFMMDDVLLAGERAKAKKPDNWEIVGKPQSQEAYGCMLRKDDPQFKK
LMDDTIAQVQTSGEAEKWFDKWFKN**PILV**EHVAFGSEDIENTLAKMDDGQLDGLAFGAIQLDGDGNILQYNAAE
GDITGRDPKQVIGKNFFKDVAPGTDSPFYGKFKFEGVASGNLNTMFEWMIPTSRGPTKVKVHMKKALS

Protein sequence of Glu-FAST-4:

AAGSTLDKIAKNGVIVVGHRESSVPFSYYDNQQKVVGYSDYSNAIVEAVKKKLNKPDQLQVKLIPITSQNRIPLLQ
NGTFDFECGSTTNNVERQKQAAFSDTIFVVGTRLLTKKGGDIKDFANLKDKAVVVTSGTTSEVLLNKLNEEQKMM
RIISAKDHGDSFRTLESGRAVAFMMDDVLLAGERAKAKKPDNWEIVGKPQSQEAYGCMLRKDDPQFKKLMDD
TIAQVQTSGEAEKWFDKWFKN**PILV**GDSYWVFKR**GGSE**HVAFGSEDIENTLAKMDDGQLDGLAFGAIQLDGD
GNILQYNAAEGDITGRDPKQVIGKNFFKDVAPGTDSPFYGKFKFEGVASGNLNTMFEWMIPTSRGPTKVKVHM
KALS**NPLNLMNFELSDMKALFKEPNDKALK**

Protein sequence of cpGlu-FAST-4:

EHVAFGSEDIENTLAKMDDGQLDGLAFGAIQLDGDGNILQYNAAEGDITGRDPKQVIGKNFFKDVAPGTDSPFYG
KFKFEGVASGNLNTMFEWMIPTSRGPTKVKVHMKKALS**NPLNLMNFELSDMKALFKEPNDKALKGGSHHHHHH**
GMASMTGGQQMGRDLYDDDDKDPGSSGSAAGSTLDKIAKNGVIVVGHRESSVPFSYYDNQQKVVGYSDYS
NAIVEAVKKKLNKPDQLQVKLIPITSQNRIPLLQNGTFDFECGSTTNNVERQKQAAFSDTIFVVGTRLLTKKGGDIK

FANLKDKAVVVTSGTTSEVLLNKLNEEQKMMNRIISAKDHGDSFRTLESGRAVAFMMDDVLLAGERAKAKKPDN
WEIVGK PQSQEAYGCMLRKDDPQFKKLMDDTIAQVQTSGEAEKWFDKWFKNPI**LV**GD SYWVFKRV

Protein sequence of Glu-FAST-2.1:

DSYWVFKRV**AAG**STLDKIAKNGVIVVGHRESSVPFSYYDNQQKVVGYSDYSNAIVEAVKKKLNKPDQLQVKLIPI
TSQNRIPLLQNGTFDFECGSTTNNVERQKQAAFSDTIFVVGTRLLTKKGGDIKDFANLKDKAVVVTSGTTSEVLLN
KLNEEQKMMNRIISAKDHGDSFRTLESGRAVAFMMDDVLLAGERAKAKKPDNWEIVGK PQSQEAYGCMLRKDD
PQFKKLMDDTIAQVQTSGEAEKWFDKWFKNPIPP**KNLNMNFELSD**EMKAL**FK**EPNDKAL**KP**PEHVAFGSEDIEN
TLAKMDDGQLDGLAFGAIQLDGDGNILQYNAAEGDITGRDPKQVIGKNFFKDVAPGTDSPFYGKFKKEGVASGN
LNTMFEWMIPTSRGPTKVKVHMKKALS

Protein sequence of K⁺-FAST-1:

EHVAFGSEDIENLAKMDDGQLDGLAFGAIQLDGDGNILQYNAAEGDITGRDPKQVIGKNFFKDVAPGTDSPFYG
GKFKKEGVASGNLNTMFEWMIPTSRGPTKVKVHMKKALS**GGMGLFNFVKDAGEKLWDAVTGQHDKDDQAKKVQ**
EHLNKTGIPDADKVNIQIADGKATVTGDGLS**QEAKEKILVAVGNISGIASVDDQVKTATPATASQFYTVKSGD**LSAI
SKQVYGNANLYNKIFEANKPMLKSPDKIYPGQVLRIP**EEGG**DSYWVFKRV

Protein sequence of K⁺-FAST-2:

GDSYWVFKRV**GGMGLFNFVKDAGEKLWDAVTGQHDKDDQAKKVQEHLNKTGIPDADKVN**IQIADGKATVTGD
GLS**QEAKEKILVAVGNISGIASVDDQVKTATPATASQFYTVKSGD**LSAIS**KQVYGNANLYNKIFEANKPMLKSPDKI**
YPGQVLRIP**EEGG**EHVAFGSEDIENLAKMDDGQLDGLAFGAIQLDGDGNILQYNAAEGDITGRDPKQVIGKNFF
KDVAPGTDSPFYGKFKKEGVASGNLNTMFEWMIPTSRGPTKVKVHMKKALS

Protein sequence of K⁺-FAST-3:

MGLFNFVKDAGEKLWDAVTGQHDKDDQAKKVQEHLNKTGIPDADKVNIQIADGKATVTGDGLS**QEAKEKILVAVG**
NISGIASVDDQVKTATPATEHVAFGSEDIENLAKMDDGQLDGLAFGAIQLDGDGNILQYNAAEGDITGRDPKQVI
GKNFFKDVAPGTDSPFYGKFKKEGVASGNLNTMFEWMIPTSRGPTKVKVHMKKALS**SGDSYWVFKRVASQFYT**
VKSGDLSAIS**KQVYGNANLYNKIFEANKPMLKSPDKIYPGQVLR**IP**EE**

Protein sequence of K⁺-FAST-4:

MGLFNFVKDAGEKLWDAVTGQHDKDDQAKKVQEHLNKTGIPDADKVNIQIADGKATVTGDGLS**QEAKEKILVAVG**
NISGIASVDDQVKTATPATGDSYWVFKRV**GGSE**EHVAFGSEDIENLAKMDDGQLDGLAFGAIQLDGDGNILQYN
AAEGDITGRDPKQVIGKNFFKDVAPGTDSPFYGKFKKEGVASGNLNTMFEWMIPTSRGPTKVKVHMKKALS**ASQ**
FYTVKSGDLSAIS**KQVYGNANLYNKIFEANKPMLKSPDKIYPGQVLR**IP**EE**

Protein sequence of K⁺-FAST-5:

GDSYWVFKRV**GGMGLFNFVKDAGEKLWDAVTGQHDKDDQAKKVQEHLNKTGIPDADKVN**IQIADGKATVTGD
GLS**QEAKEKILVAVGNISGIASVDDQVKTATPATASGGGGSGGGGSGGGGS**QFYTVKSGDLSAIS**KQVYGNANL**
YNKIFEANKPMLKSPDKIYPGQVLRIP**EEGG**EHVAFGSEDIENLAKMDDGQLDGLAFGAIQLDGDGNILQYNAAE
GDITGRDPKQVIGKNFFKDVAPGTDSPFYGKFKKEGVASGNLNTMFEWMIPTSRGPTKVKVHMKKALS

Protein sequence of K⁺-FAST-5.1:

DSYWVFKRV**GGMGLFNFVKDAGEKLWDAVTGQHDKDDQAKKVQEHLNKTGIPDADKVN**IQIADGKATVTGDG
LS**QEAKEKILVAVGNISGIASVDDQVKTATPATASGGGGSGGGGSGGGGS**QFYTVKSGDLSAIS**KQVYGNANLY**
NKIFEANKPMLKSPDKIYPGQVLRIP**EEGG**EHVAFGSEDIENLAKMDDGQLDGLAFGAIQLDGDGNILQYNAAE
GDITGRDPKQVIGKNFFKDVAPGTDSPFYGKFKKEGVASGNLNTMFEWMIPTSRGPTKVKVHMKKALS

Protein sequence of ATP-FAST-1:

EHVAFGSEDIENLAKMDDGQLDGLAFGAIQLDGDGNILQYNAAEGDITGRDPKQVIGKNFFKDVAPGTDSPFYG
GKFKKEGVASGNLNTMFEWMIPTSRGPTKVKVHMKKALS**KTIHVS**VTPDGPVYEDDVEMVSVKAKSGELGILPG
HIPLKAPLEISAARLKKGGKTQYIAVSGGNLEVRPKV**TIYAQAAERAEDIDVLR**AKAAKERAERRLQSQQDDIDF
KRAELALKRAMNRLSVAEMKGDSYWVFKRV

Protein sequence of ATP-FAST-2:

GDSYWVFKRV**KTIHVS**VTPDGPVYEDDVEMVSVKAKSGELGILPG**HIPLKAPLEISAARLKKGGKTQYIAVSG**
GNLEVRPKV**TIYAQAAERAEDIDVLR**AKAAKERAERRLQSQQDDIDF**KRAELALKRAMNRLSVAEMK**EHVAFGS
EDIENLAKMDDGQLDGLAFGAIQLDGDGNILQYNAAEGDITGRDPKQVIGKNFFKDVAPGTDSPFYGKFKKEGV
ASGNLNTMFEWMIPTSRGPTKVKVHMKKALS

Protein sequence of ATP-FAST-3:

KTIHVSVVTPDGPVYEDDVEMVSVKAKSGELGILPGHIPLKAPLEISAARLKKGGKTQYIAVSGGNLEVRPDKVTIY
AQAERAEDIDVLRAKAAKERAERRLSQQEHVAFGSEDIENLAKMDDGQLDGLAFGAIQLDGDGNILQYNAA
EGDITGRDPKQVIGKNFFKDVAPGTDSPFYGKFKKEGVASGNLNTMFEWMIPTSRGPTKVKVHMKKALS
GDSYVWFVVKRVIDFKRAELALKRAMNRLSVAEMK

Protein sequence of ATP-FAST-4:

KTIHVSVVTPDGPVYEDDVEMVSVKAKSGELGILPGHIPLKAPLEISAARLKKGGKTQYIAVSGGNLEVRPDKVTIY
AQAERAEDIDVLRAKAAKERAERRLSQQGDSYVWFVVKRV**GGSE**HVAFGSEDIENLAKMDDGQLDGLAFGA
IQLDGDGNILQYNAAEGDITGRDPKQVIGKNFFKDVAPGTDSPFYGKFKKEGVASGNLNTMFEWMIPTSRGPTKV
KVHMKKALSIDFKRAELALKRAMNRLSVAEMK

Protein sequence of ATP-pFAST-1:

EHVAFGSEDIENLANMDDQLDRLAFGVIQLDGDGNILLYNAAEGDITGRDPKQVIGKNFFKDVAPGTDTPFYG
KFKEGAASGNLNTMFEWTIPTSRGPTKVKVHLKALS**KTIHVSVVTPDGPVYEDDVEMVSVKAKSGELGILPGHI
PLKAPLEISAARLKKGGKTQYIAVSGGNLEVRPDKVTIYAQAERAEDIDVLRAKAAKERAERRLSQQDDIDFKR
AELALKRAMNRLSVAEMK**GDRYWVFKRV

Protein sequence of mCherry-ATP-FAST-1:

MASVSKGEEDNMAIIKEFMRFKVHMEGSVNGHEFEIEGEGEGRPYEGTQTAKLKVTKGGPLPFAWDILSPQFMY
GSKAYVKHPADIPDYLKLSFPEGFKWERVMNFEDGGVTVTQDSSLQDGEFIYKVKLRGTNFPDGPVMQKKT
MGWEASSERMYPEDGALKGEIKQRLKLDGGHYDAEVKTTYKAKKPVQLPGAYNVNIKLDITSHNEDYTIVEQY
ERAEGRHSTGGMDELYK**SGGGGSGGGGSE**HVAFGSEDIENLAKMDDGQLDGLAFGAIQLDGDGNILQYNAAE
GDITGRDPKQVIGKNFFKDVAPGTDSPFYGKFKKEGVASGNLNTMFEWMIPTSRGPTKVKVHMKKALS**KTIHVSV
VTPDGPVYEDDVEMVSVKAKSGELGILPGHIPLKAPLEISAARLKKGGKTQYIAVSGGNLEVRPDKVTIYAQAER
AEDIDVLRAKAAKERAERRLSQQDDIDFKRAELALKRAMNRLSVAEMK**GDSYVWFVVKRV

Protein sequence of mCherry-ATP-pFAST-1:

MASVSKGEEDNMAIIKEFMRFKVHMEGSVNGHEFEIEGEGEGRPYEGTQTAKLKVTKGGPLPFAWDILSPQFMY
GSKAYVKHPADIPDYLKLSFPEGFKWERVMNFEDGGVTVTQDSSLQDGEFIYKVKLRGTNFPDGPVMQKKT
MGWEASSERMYPEDGALKGEIKQRLKLDGGHYDAEVKTTYKAKKPVQLPGAYNVNIKLDITSHNEDYTIVEQY
ERAEGRHSTGGMDELYK**SGGGGSGGGGSE**HVAFGSEDIENLANMDDQLDRLAFGVIQLDGDGNILLYNAAE
GDITGRDPKQVIGKNFFKDVAPGTDTPFYGKFKKEGAASGNLNTMFEWTIPTSRGPTKVKVHLKALS**KTIHVSV
VTPDGPVYEDDVEMVSVKAKSGELGILPGHIPLKAPLEISAARLKKGGKTQYIAVSGGNLEVRPDKVTIYAQAER
AEDIDVLRAKAAKERAERRLSQQDDIDFKRAELALKRAMNRLSVAEMK**GDRYWVFKRV

Text S1. Theoretical model for the analysis of allosteric fluorogenic biosensors

The following theoretical model for the analysis of allosteric fluorogenic biosensors was adapted from Velazquez-Campoy et al.⁵

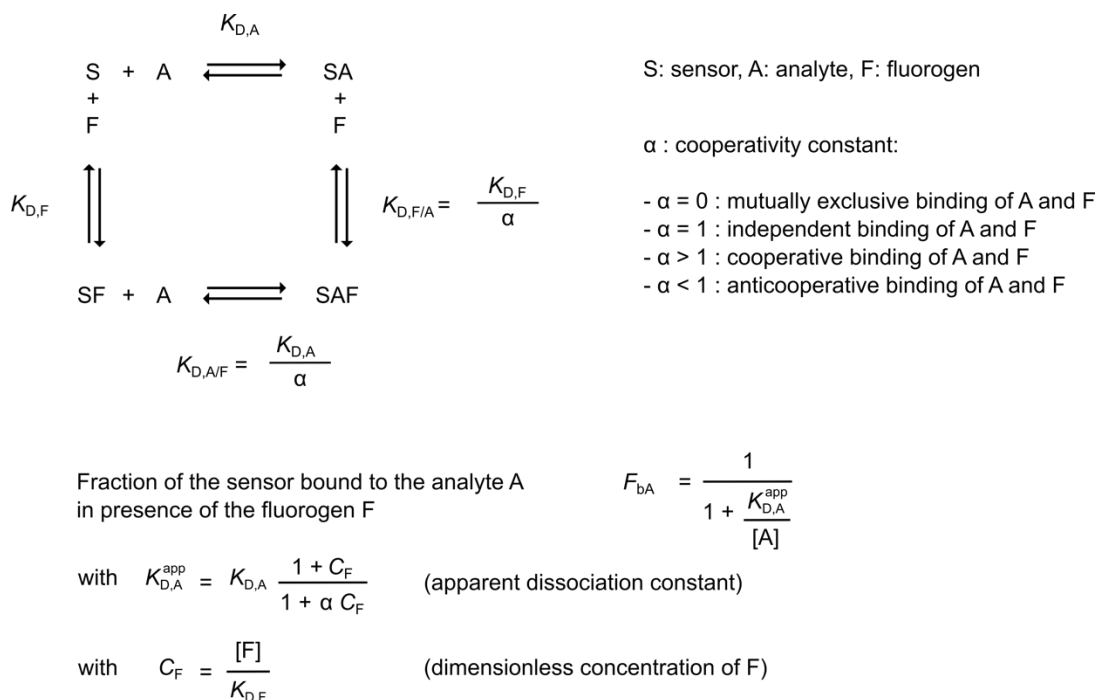


Figure S1. Model for the binding of a fluorogen F and an analyte A to two binding sites far apart in the sensor S, but coupled by a conformational change induced by the binding of either ligand and having an effect on the binding of the other ligand. Adapted from Velazquez-Campoy et al.⁵

Fig. S1 shows the general scheme of the ternary equilibrium in which the sensor S is able to bind the fluorogen F and the analyte A and form a ternary complex SFA. $K_{D,A}$ and $K_{D,F}$ are the dissociation constant for the binding of A and F:

$$K_{D,A} = \frac{[S][A]}{[SA]} \quad (1)$$

$$K_{D,F} = \frac{[S][F]}{[SF]} \quad (2)$$

and $K_{D,A/F}$ and $K_{D,F/A}$ are the dissociation constants for the analyte A and the fluorogen F when the sensor S is already bound to the fluorogen F and the analyte A respectively:

$$K_{D,A/F} = \frac{[SF][A]}{[SFA]} \quad (3)$$

$$K_{D,F/A} = \frac{[SA][F]}{[SFA]} \quad (4)$$

If the binding of the analyte A influences the binding of the fluorogen F, one can introduce a cooperativity constant α for the binding of F when A is bound to the macromolecule:

$$K_{D,F/A} = \frac{K_{D,F}}{\alpha} \quad (6)$$

According to equations (1-4)

$$K_{D,F} K_{D,A/F} = K_{D,A} K_{D,F/A} \quad (5)$$

Thus, it can be concluded that

$$K_{D,A/F} = \frac{K_{D,A}}{\alpha} \quad (7)$$

Therefore, the influence between the two ligands is reciprocal: if the binding of the analyte A modifies the binding affinity of the fluorogen F, the binding of the fluorogen F modifies the binding affinity of the analyte A in the same extent.

Different cases are thus possible. If $\alpha = 0$, the formation of the ternary complex is not possible (case of competitive ligands or mutually exclusive binding). If $\alpha = 1$, the formation of the ternary complex is possible, but the binding of one ligand has no influence on the binding of the other type of ligand (independent binding of the two ligands). If $\alpha > 1$, the formation of the ternary complex is possible, and the binding of one type of ligand raises the binding affinity of the other type of ligand (positive cooperative binding). If $\alpha < 1$, the formation of the ternary complex is possible, but the binding of one type of ligand lowers the binding affinity of the other type of ligand (negative cooperative binding).

The ternary system can be substituted to an equivalent binary system in which the fluorogen F implicitly influences the binding of the analyte A (through apparent thermodynamic parameters). This enables to analyze titrations of the sensor S with the analyte A according to the standard procedure for a single ligand binding to a macromolecule. Indeed, the fraction of sensor S bound to the analyte A is given by:

$$F_{bA} = \frac{[SA] + [SFA]}{[S] + [SA] + [SF] + [SFA]} \quad (8)$$

$$= \frac{\frac{[A]}{K_{D,A}} + \alpha \frac{[A][F]}{K_{D,A}K_{D,F}}}{1 + \frac{[A]}{K_{D,A}} + \frac{[F]}{K_{D,F}} + \alpha \frac{[A][F]}{K_{D,A}K_{D,F}}} \quad (9)$$

which can be reduced to a simpler expression if an apparent dissociation constant is defined:

$$F_{bA} = \frac{1}{1 + \frac{K_{D,A}^{app}}{[A]}} \quad (10)$$

where:

$$K_{D,A}^{\text{app}} = K_{D,A} \frac{1 + \frac{[F]}{K_{D,F}}}{1 + \alpha \frac{[F]}{K_{D,F}}} \quad (11)$$

Using the dimensionless concentration $C_F = [F]/K_{D,F}$, one gets

$$K_{D,A}^{\text{app}} = K_{D,A} \frac{1 + C_F}{1 + \alpha C_F} \quad (12)$$

Note that $K_{D,A}^{\text{app}} = K_{D,A}$ when $C_F = 0$ (absence of fluorogen) and $K_{D,A}^{\text{app}} = K_{D,A}/\alpha$ when C_F is sufficiently high to saturate the sensor.

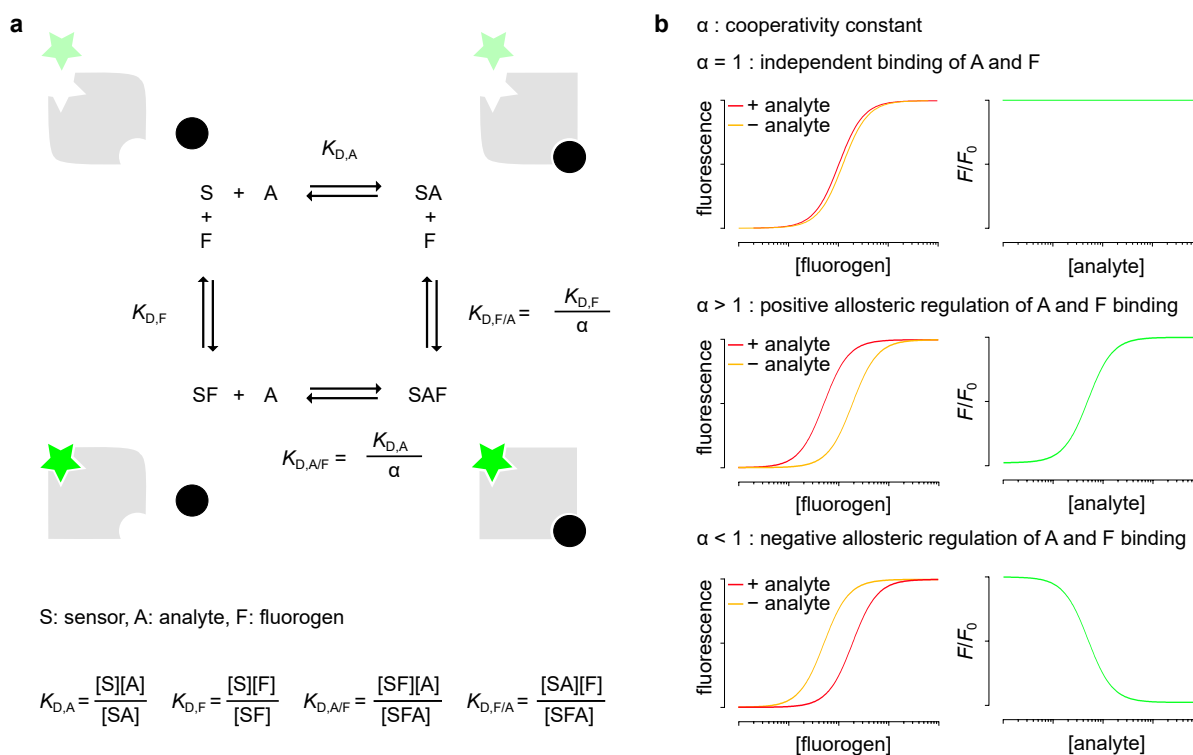


Figure S2. Theoretical model for describing allosteric fluorogenic protein sensor. (a) Thermodynamic box. (b) Theoretical possible behaviors. Here we assume that the brightness of SF and SAF are similar.

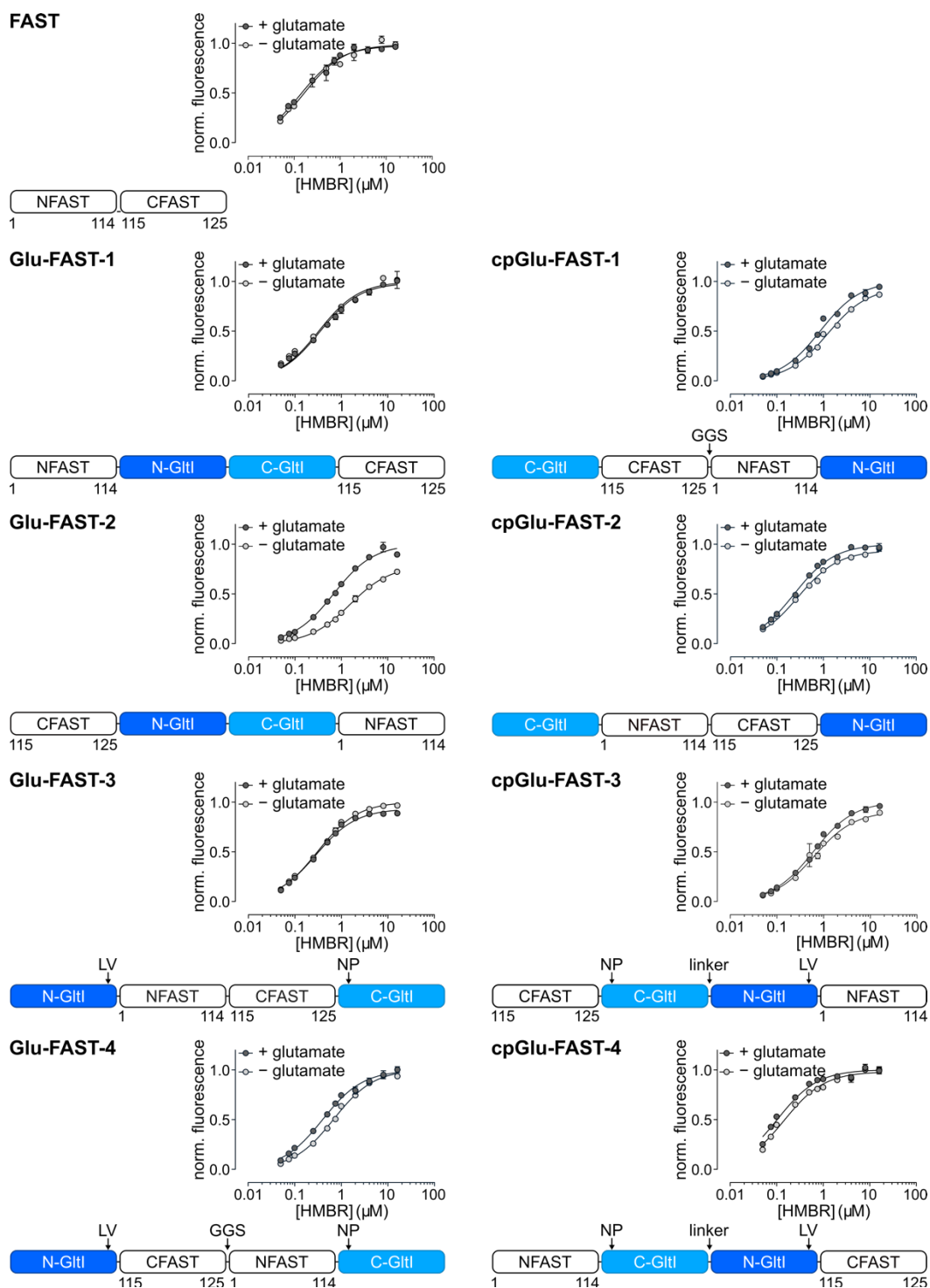


Figure S3. Study of different topologies for the design of FAST-based glutamate biosensors. HMBR titration curves of the eight Glutamate-responsive FAST topologies, in absence (light grey) and in presence of 5 mM glutamate (dark grey) in pH 7.4 HEPES buffer (50 mM) containing NaCl (150 mM). Data represent the mean \pm sem ($n = 3$). The least-squares fit (line) gave the thermodynamic dissociation constants $K_{D,HMBR}$ and $K_{D,HMBR/glutamate}$ provided in **Table S1**. The sensor concentration was fixed at 0.1 μM .

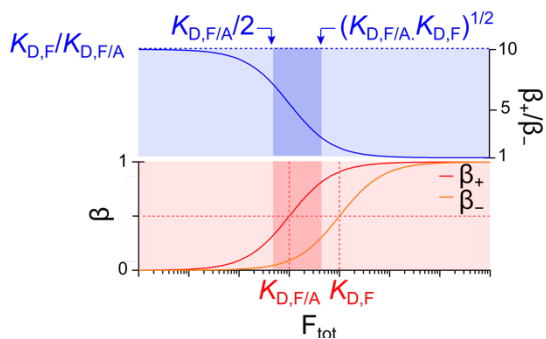
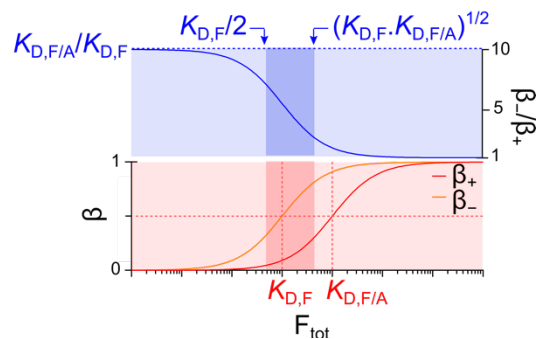
a positive allosteric regulation**b negative allosteric regulation**

Figure S4. How to choose fluorogen concentration to obtain both good dynamic range and satisfactory detection sensitivity. **a** Simulated fluorogen binding curves in the presence and absence of analyte (with $K_{D,F} = 10 K_{D,F/A}$) in the case of a positive allosteric regulation. β_+ and β_- are the fluorogen bound fractions in presence and absence of the analyte, respectively. Choosing the concentration of fluorogen F_{tot} between $K_{D,F/A} / 2$ and $(K_{D,F/A} \cdot K_{D,F})^{1/2}$ (contrasted rectangles) is a good compromise to obtain both good dynamic range and satisfactory detection sensitivity. **b** Simulated fluorogen binding curves in the presence and absence of analyte (with $K_{D,F/A} = 10 K_{D,F}$) in the case of a negative allosteric regulation. β_+ and β_- are the fluorogen bound fractions in presence and absence of the analyte, respectively. Choosing the concentration of fluorogen between $K_{D,F}/2$ and $(K_{D,F} \cdot K_{D,F/A})^{1/2}$ (contrasted rectangles) is a good compromise to obtain both good dynamic range and satisfactory detection sensitivity. Adapted from Tebo et al.⁶

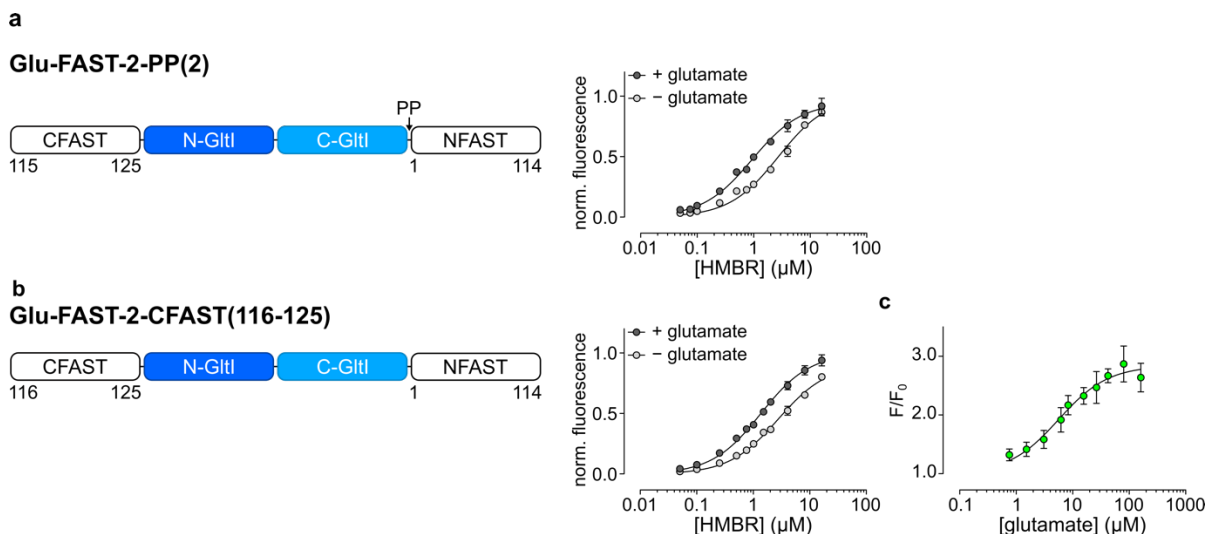


Figure S5. Optimization steps of Glu-FAST-2. **a,b** HMBR titration curves of Glu-FAST-2-PP(2) (**a**) and Glu-FAST-2-CFAST(116-125) (**b**), respectively, in absence (light grey) and in presence of 5 mM glutamate (dark grey) in pH 7.4 HEPES buffer (50 mM) containing NaCl (150 mM). **c** Glutamate titration curve of Glu-FAST-2-CFAST(116-125) in the presence of 1 μ M HMBR in pH 7.4 HEPES buffer (50 mM) containing NaCl (150 mM). Data represent the mean \pm sem ($n = 3$). The least-squares fit (line) gave the thermodynamic dissociation constants $K_{D,HMBR}$, $K_{D,HMBR/glutamate}$ and $K_{D,glutamate\ app}$ provided in **Table S2**. The sensor concentration was fixed at 0.1 μ M.

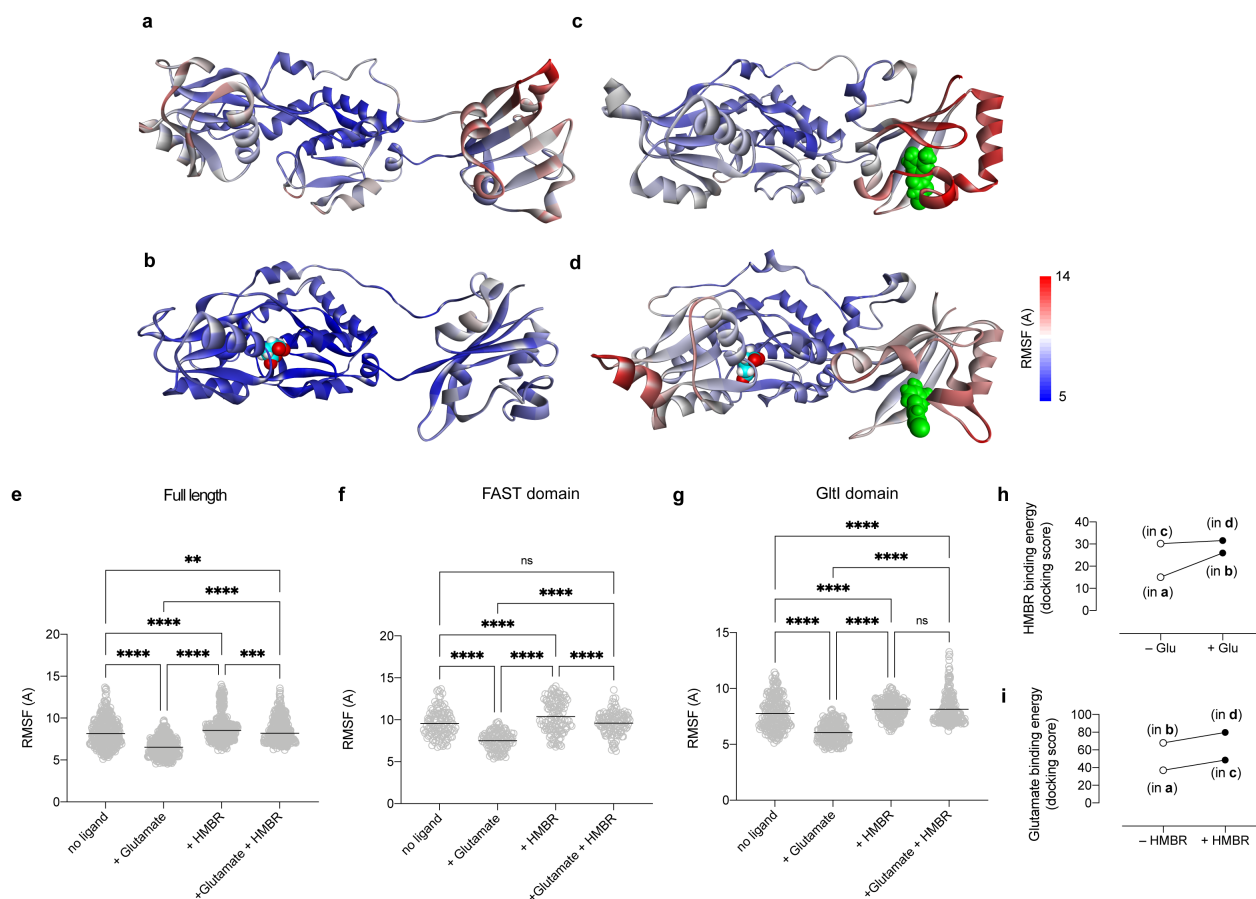
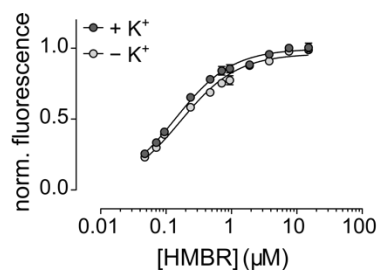
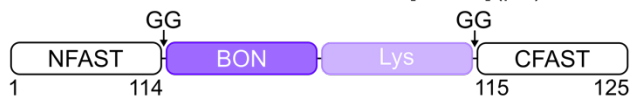
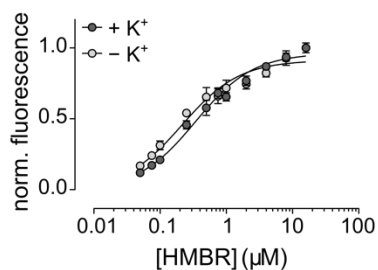


Figure S6. Study of Glu-FAST-2.1 by molecular dynamics. (a-d) Conformation of Glu-FAST-2.1 models without ligand (a), with glutamate (b), with HMBR (c) and with both ligands (d) obtained after molecular dynamic simulations of 30 ns. HMBR (green) and glutamate are shown in space-filling model. Root mean square fluctuations (RMSF) of the residues are color coded according to the shown color scale. (e-g) RMSF of each residue in function of the ligands that are present for the full-length sensor (e), the FAST domain (f) and the GltI domain (g). The black lines show the mean RMSF in each condition; statistical comparisons were done via a 2-way ANOVA. (h) Estimation of the HMBR binding energy in absence or in presence of Glutamate through HMBR docking in the optimized structures (a) and (b), or by HMBR redocking in the optimized structure (c) and (d). The docking scores are given. (i) Estimation of the relative Glutamate binding energy in absence or in presence of HMBR through Glutamate docking in the optimized structures (a) and (c), or by Glutamate redocking in the optimized structures (b) and (d). The docking scores are given.

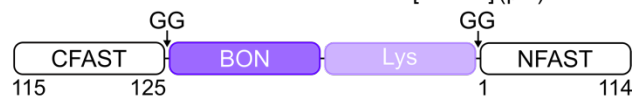
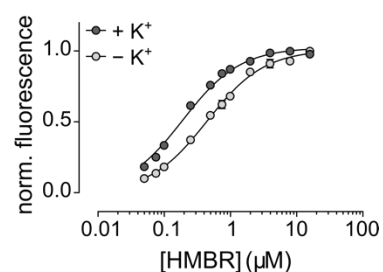
FAST



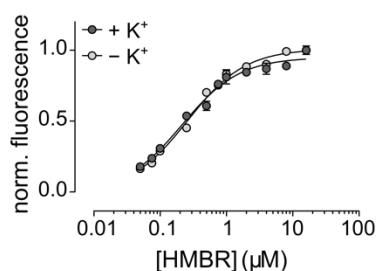
K⁺-FAST-1



K⁺-FAST-2



K⁺-FAST-3



K⁺-FAST-4

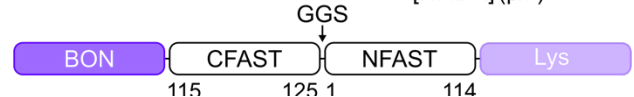
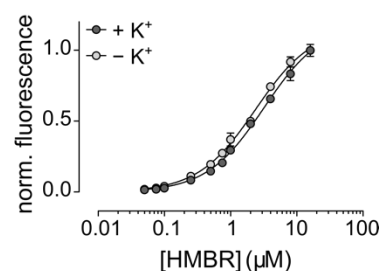


Figure S7. Study of different topologies for the design of FAST-based K⁺ biosensors. HMBR titration curves of the four K⁺-responsive FAST topologies, in absence (light grey) and in presence of 10 mM K⁺ (dark grey) in pH 7.4 HEPES buffer (50 mM) containing MgCl₂ (75 mM). Data represent the mean ± sem (n = 3). The least-squares fit (line) gave the thermodynamic dissociation constants $K_{D,HMBR}$ and $K_{D,HMBR/K^+}$ provided in **Table S3**. The sensor concentration was fixed at 0.1 μM.

K⁺-FAST-5

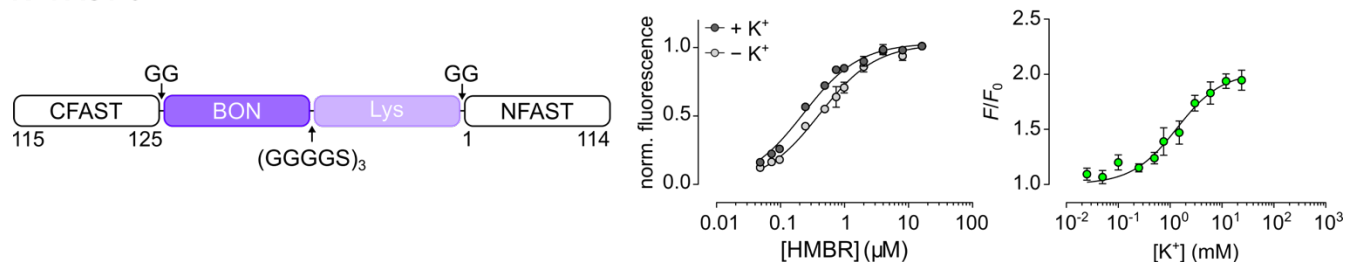


Figure S8. Characterization of K⁺-FAST-5. **a** HMBR titration curves of K⁺-FAST-5 in absence (light grey) and in presence of 100 mM K⁺ (dark grey) in pH 7.4 HEPES buffer (50 mM) containing MgCl₂ (75 mM). **b** K⁺ titration curve of K⁺-FAST-5 in the presence of 0.1 μM HMBR in pH 7.4 HEPES buffer (50 mM) containing MgCl₂ (75 mM). Data represent the mean ± sem (n = 3). The least-squares fit (line) gave the thermodynamic dissociation constants $K_{D,HMBR}$, $K_{D,HMBR/K^+}$ and $K_{D,K^+ app}$ provided in **Table S4**. The sensor concentration was fixed at 0.1 μM.

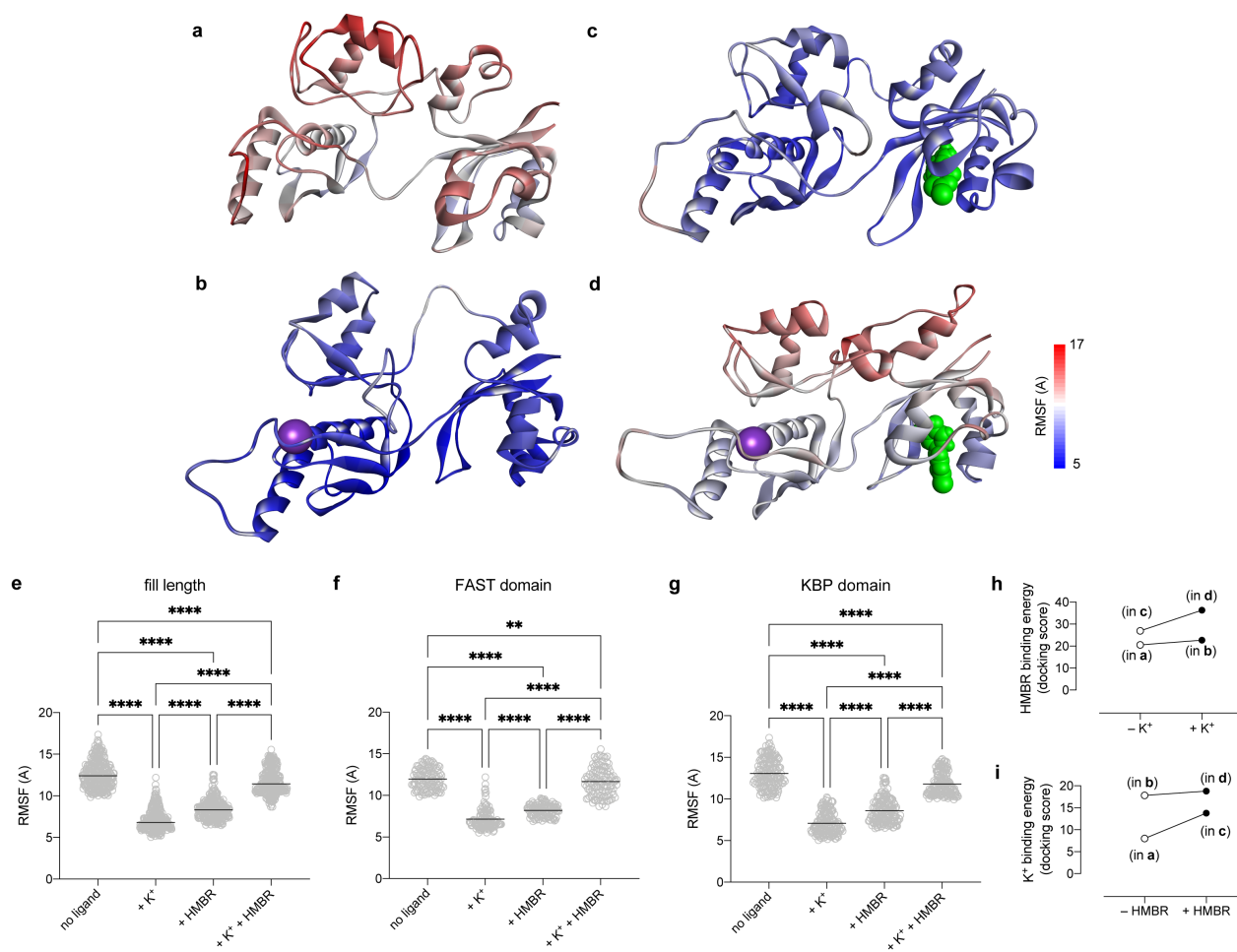


Figure S9. Study of K⁺-FAST-5.1 by molecular dynamics. (a-d) Conformation of K⁺-FAST-5.1 models without ligand (a), with K⁺ (b), with HMBR (c) and with both ligands (d) obtained after molecular dynamic simulations of 30 ns. HMBR (green) and K⁺ (violet) are shown in space-filling model. Root mean square fluctuations (RMSF) of the residues are color coded according to the shown color scale. (e-g) RMSF of each residue in function of the ligands that are present for the full-length sensor (e), the FAST domain (f) and the Kbp domain (g). The black lines show the mean RMSF in each condition; statistical comparisons were done via a 2-way ANOVA. (h) Estimation of the HMBR binding energy in absence or in presence of K⁺ through HMBR docking in the optimized structures (a) and (b), or by HMBR redocking in the optimized structure (c) and (d). The docking scores are given. (i) Estimation of the relative K⁺ binding energy in absence or in presence of HMBR through K⁺ docking in the optimized structures (a) and (c), or by K⁺ redocking in the optimized structures (b) and (d). The docking scores are given.

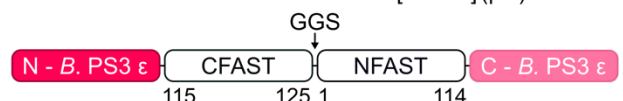
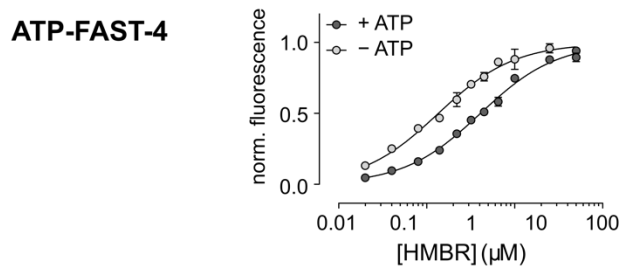
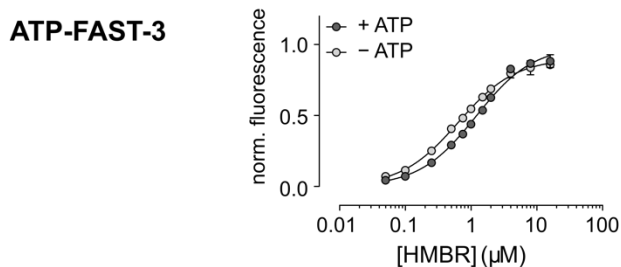
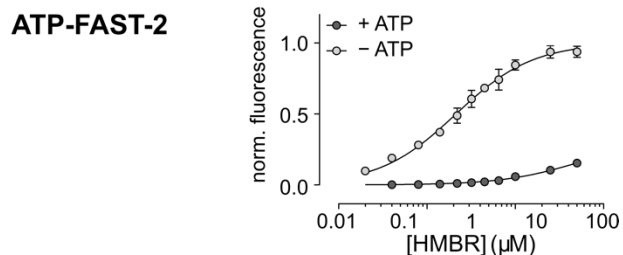
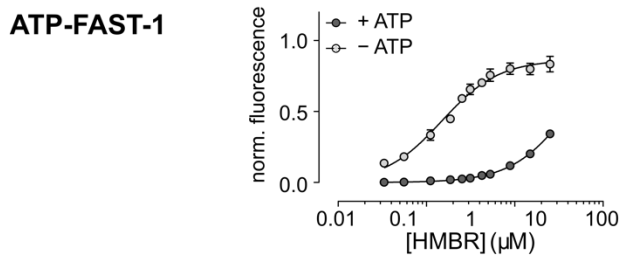


Figure S10. Study of different topologies for the design of FAST-based ATP biosensors. HMBR titration curves of the four ATP-responsive FAST topologies, in absence (light grey) and in presence of 5 mM ATP (dark grey) in pH 7.4 HEPES buffer (50 mM) containing $MgCl_2$ (75 mM). Data represent the mean \pm sem ($n = 3$). The least-squares fit (line) gave the thermodynamic dissociation constants $K_{D,HMBR}$ and $K_{D,HMBR/ATP}$ provided in **Table S5**. The sensor concentration was fixed at 0.1 μM .

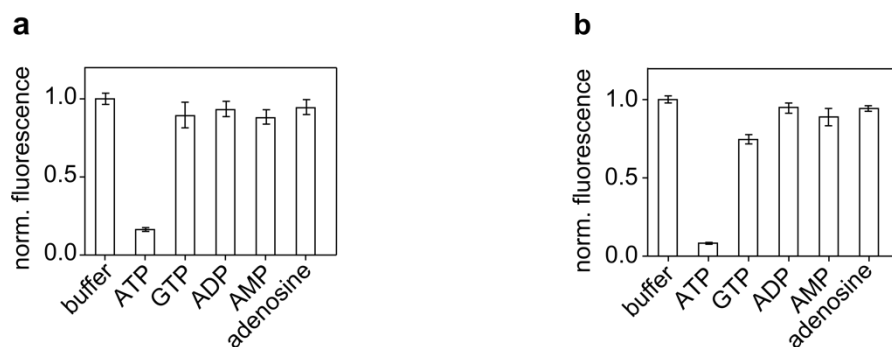
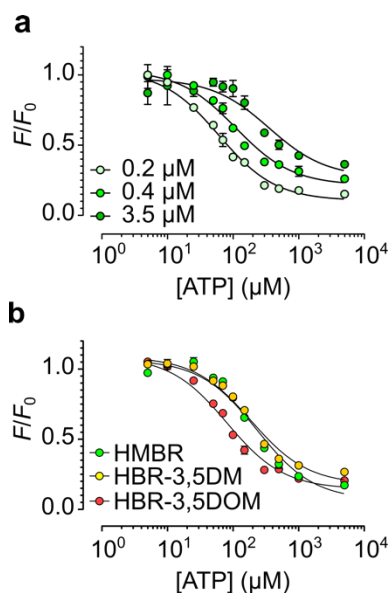


Figure S11. ATP selectivity. **a** Normalized fluorescence intensity upon addition to ATP-FAST-1 of ATP and analogs at concentration = $10 K_{D,ATP\ app} = 1.2$ mM in the presence of $0.4\ \mu\text{M}$ HMBR. **b** Normalized fluorescence intensity upon addition to ATP-pFAST-1 of ATP and analogs at concentration = $10 K_{D,ATP\ app} = 7$ mM in the presence of $0.1\ \mu\text{M}$ HMBR. Data represent the mean \pm sem ($n = 3$). The sensor concentration was fixed at $0.1\ \mu\text{M}$.



c

Fluorogen	[fluorogen] (μM)	$K_{D,ATP\ app}$ (μM)
HMBR	0.2	61 \pm 9
	0.4	110 \pm 21
	3.5	350 \pm 130
HBR-3,5DM	1	230 \pm 55
	1	190 \pm 33
HBR-3,5DOM	1	80 \pm 14

Figure S12. Modularity provided by varying the fluorogen with ATP-FAST-1 **a** ATP titration curves of ATP-FAST-1 in pH 7.4 HEPES buffer (50 mM) containing MgCl_2 (75 mM), in the presence of 0.2, 0.4 and 3.5 μM HMBR. **b** ATP titration curves of ATP-FAST-1 in the presence of 1 μM HMBR (green), HBR-3,5DM (yellow) and HBR-3,5DOM (red), in pH 7.4 HEPES buffer (50 mM) containing MgCl_2 (75 mM). Data represent the mean \pm sem ($n = 3$). The least-squares fit (line) gave the thermodynamic dissociation constants $K_{D,ATP\ app}$ provided in **c**. The sensor concentration was fixed at 0.1 μM . **c** The apparent dissociation constant $K_{D,ATP\ app}$ for ATP binding with ATP-FAST-1 is given for each fluorogen at various concentrations.

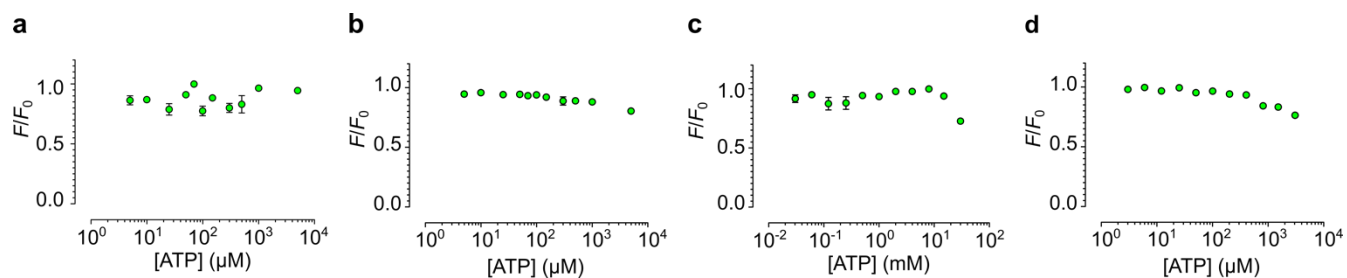


Figure S13. ATP responsiveness. **a** ATP titration curve of FAST in the presence of 0.1 μM HMBR, in pH 7.4 HEPES buffer (50 mM) containing MgCl_2 (75 mM). **b** ATP titration curves of insensitive ATP-FAST-1-R122K/R126K, in the presence of 0.4 μM HMBR. **c** ATP titration curve of pFAST in the presence of 0.1 μM HMBR in pH 7.4 HEPES buffer (50 mM) containing MgCl_2 (75 mM). **d** ATP titration curves of insensitive ATP-pFAST-1-R122K/R126K, in the presence of 0.1 μM HMBR. Data represent the mean \pm sem ($n = 3$). The sensor concentration was fixed at 0.1 μM .

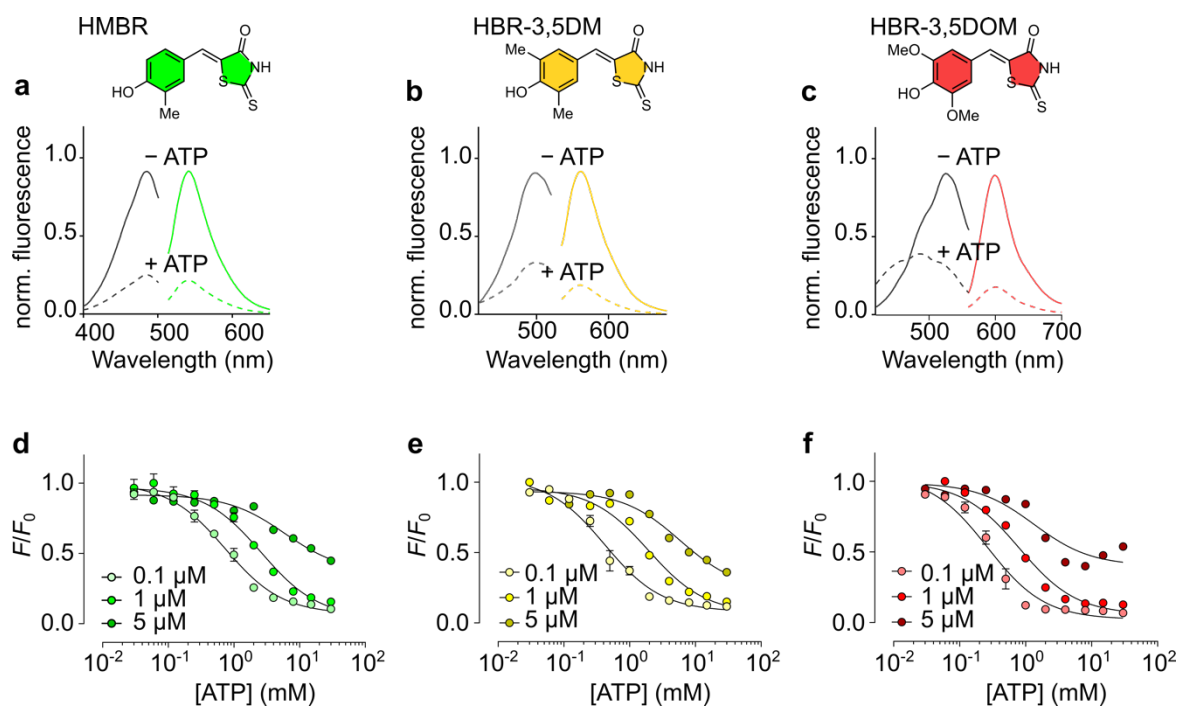


Figure S14. Modularity provided by varying the fluorogen with ATP-pFAST-1. a-c Excitation and emission spectra of ATP-pFAST-1 with a HMBR, b HBR3,5DM and c HBR3,5DOM in the absence (solid line) and in the presence of 30 mM ATP (dotted line). The concentration of fluorogen was 1 μM . Sensor concentration was fixed at 0.1 μM . d-f ATP titration curves of ATP-pFAST-1 in presence of 0.1, 1 or 5 μM of d HMBR, e HBR-3,5-DM and f HBR-3,5-DOM, in pH 7.4 HEPES buffer (50 mM) containing MgCl_2 (75 mM). Data represent the mean \pm sem ($n = 3$). The least-squares fit (line) gave the thermodynamic dissociation constant $K_{D,ATP\text{ app}}$ provided in Table S6. The sensor concentration was fixed at 0.1 μM .

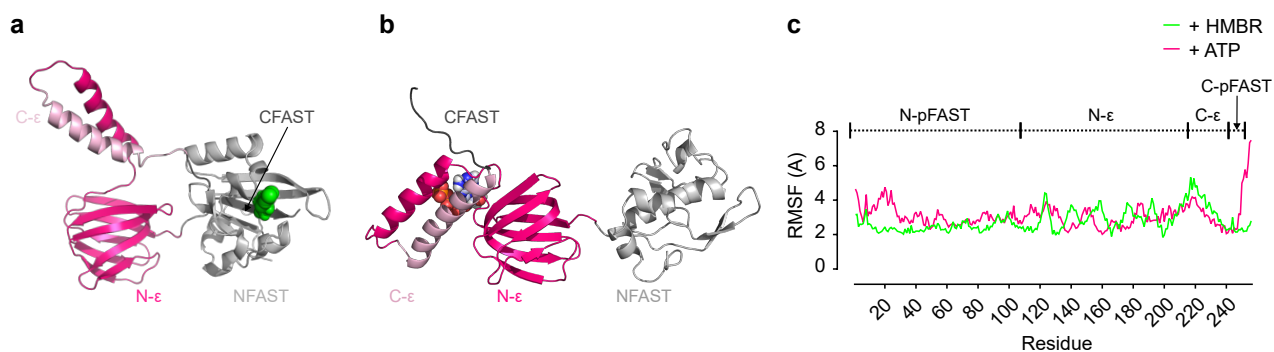


Figure S15. Structural models of ATP-pFAST-1. a,b Structural models of ATP-pFAST-1 bound to ATP (a) or HMBR (b) generated by homology modeling and molecular dynamics. B. PS3 ϵ is in magenta and pFAST in grey. HMBR and ATP are shown in space-filling model. c Root mean square fluctuations (RMSF) of the residues of ATP-pFAST-1 during molecular dynamic simulations of 2 ns.

Table S1. Study of different topologies for the design of FAST-based glutamate biosensors. For each sensor is given the dissociation constant of HMBR in absence of glutamate ($K_{D,HMBR}$), in presence of 5 mM of glutamate ($K_{D,HMBR/glutamate}$), and the cooperativity constant α , calculated as the ratio $K_{D,HMBR}/K_{D,HMBR/glutamate}$.

Sensor	$K_{D,HMBR}$ (μM)	$K_{D,HMBR/glutamate}$ (μM)	α
FAST	0.14 \pm 0.01	0.16 \pm 0.01	0.9
Glu-FAST-1	0.33 \pm 0.04	0.34 \pm 0.03	1.0
cpGlu-FAST-1	1.2 \pm 0.08	0.86 \pm 0.08	1.4
Glu-FAST-2	1.5 \pm 0.05	0.68 \pm 0.05	2.2
cpGlu-FAST-2	0.28 \pm 0.02	0.24 \pm 0.01	1.2
Glu-FAST-3	0.31 \pm 0.01	0.28 \pm 0.02	1.1
cpGlu-FAST-3	0.63 \pm 0.06	0.61 \pm 0.03	1.0
Glu-FAST-4	0.68 \pm 0.04	0.40 \pm 0.02	1.7
cpGlu-FAST-4	0.14 \pm 0.01	0.10 \pm 0.01	1.4

Table S2. Optimization steps of Glu-FAST-2. For each sensor is given the dissociation constant of HMBR in absence of glutamate ($K_{D,HMBR}$), in presence of 5 mM of glutamate ($K_{D,HMBR/glutamate}$), and the cooperativity constant α , calculated as the ratio $K_{D,HMBR}/K_{D,HMBR/glutamate}$. The apparent dissociation constant of glutamate is also given with the associated fluorescence intensity increase observed upon glutamate addition (F_{max}/F_{min}).

Sensor	$K_{D,HMBR}$ (μM)	$K_{D,HMBR/glutamate}$ (μM)	α	$K_{D,glutamate}$ app (μM)	F_{max}/F_{min}
Glu-FAST-2-PP(2)	2.7 \pm 0.2	1.3 \pm 0.1	2.1	-	-
Glu-FAST-2-CFAST(116-125)	2.7 \pm 0.3	0.93 \pm 0.06	2.9	5.4 \pm 0.4	2.4

Table S3. Study of different topologies for the design of FAST-based K^+ biosensors. For each sensor is given the dissociation constant of HMBR in absence of K^+ ($K_{D,HMBR}$), in presence of 10 mM of K^+ ($K_{D,HMBR/K^+}$), and the cooperativity constant α , calculated as the ratio $K_{D,HMBR}/K_{D,HMBR/K^+}$.

Sensor	$K_{D,HMBR}$ (μM)	$K_{D,HMBR/K^+}$ (μM)	α
FAST	0.15 \pm 0.01	0.17 \pm 0.01	0.9
K^+ -FAST-1	0.21 \pm 0.03	0.34 \pm 0.03	0.6
K^+ -FAST-2	0.44 \pm 0.02	0.19 \pm 0.01	2.3
K^+ -FAST-3	0.26 \pm 0.02	0.21 \pm 0.02	1.2
K^+ -FAST-4	2.4 \pm 0.1	3.1 \pm 0.1	0.8

Table S4. Characterization of K⁺-FAST-5. Is given the dissociation constant of HMBR in absence of K⁺ ($K_{D,HMBR}$), in presence of 100 mM K⁺ ($K_{D,HMBR/K^+}$), and the cooperativity constant α , calculated as the ratio $K_{D,HMBR}/K_{D,HMBR/K^+}$. The apparent dissociation constant of K⁺ is also given with the associated fluorescence intensity increase observed upon K⁺ addition (F_{max}/F_{min}).

Sensor	$K_{D,HMBR}$ (μM)	$K_{D,HMBR/K^+}$ (μM)	α	$K_{D,K^+ \text{ app}}$ (mM)	F_{max}/F_{min}
K ⁺ -FAST-5	0.42 ± 0.03	0.23 ± 0.02	1.8	1.1 ± 0.3	1.9

Table S5. Study of different topologies for the design of FAST-based ATP biosensors. For each sensor is given the dissociation constant of the fluorogen in absence of ATP ($K_{D,HMBR}$), in presence of 5 mM of ATP ($K_{D,HMBR/ATP}$), and the cooperativity constant α , calculated as the ratio $K_{D,HMBR}/K_{D,HMBR/ATP}$.

Sensor	$K_{D,HMBR}$ (μM)	$K_{D,HMBR/ATP}$ (μM)	α
ATP-FAST-1	0.37 ± 0.10	~ 31	~ 0.01
ATP-FAST-2	2.1 ± 0.1	~ 52	~ 0.04
ATP-FAST-3	0.64 ± 0.02	1.2 ± 0.1	0.5
ATP-FAST-4	1.3 ± 0.1	4.0 ± 0.2	0.3

Table S6. Modularity provided by varying the fluorogen with ATP-pFAST-1. The apparent dissociation constant for ATP is given for each fluorogen with the associated fluorescence intensity decrease observed upon ATP addition (F_{max}/F_{min}).

Fluorogen	[fluorogen] (μM)	$K_{D,ATP \text{ app}}$ (mM)	F_{max}/F_{min}
HMBR	0.1	0.73 ± 0.09	9.5
	1	2.6 ± 0.6	6.4
	5	5.9 ± 2.3	2.5
HBR-3,5-DM	0.1	0.42 ± 0.07	8.5
	1	1.9 ± 0.4	6.6
	5	5.8 ± 2.2	4.0
HBR-3,5-DOM	0.1	0.26 ± 0.06	15
	1	0.80 ± 0.17	7.9
	5	1.3 ± 0.7	2.5

Table S7. Primers used in this study

Primer	Sequence
kanf	Gcatcaaccaaaccttattcattcgtg
kanr	Cacgaatgaataacggtttggtgatgc
ag336	gcagcggcggaggggatccgagcatgtgcctttggcag
ag579	Catgctagccatattggctgccg
ag601	ggcagccatattggctagcatggagcatgttcctttgg
ag607	ggcagccatattggctagcatggcagcgggcagctactctg
ag613	gtattccggaagaggcggcgggtgacagctattgggtctttg
ag614	ttgaacagaccataccaccggaaggcctttctcatgtgc
ag615	agaaagcccttccgggtgatgggtctgtcaattttgtaaag
ag616	caatagctgtcaccgccctcttccggaatacgaacac
ag617	gtattccggaagaggcggcggagcatgttcctttggc
ag618	ttgaacagaccataccaccaccgtttcacaagacc
ag619	ttgtgaacgggtgggtgatgggtctgtcaattttgtaaag
ag620	aaggcaacatgctcgcgccctcttccggaatacgaacac
ag621	gggtctttgtaaacgggtgccagccagtttataccgtaag
ag622	ctgcaaaggcaacatgctcagtggtggtgtcgc
ag623	gaaaacggcgacaccagccactgagcatgttcctttggcag
ag624	acggataaaaactggctgccaccctttcacaagacc
ag625	acatgaagaaagcccttccgagccagtttataccgtaag
ag626	aagaccaatagctgtcaccagtggtggtgtcgc
ag627	gaaaacggcgacaccagccactggtgacagctattgggtctttg
ag628	acggataaaaactggctgccggaaggcctttctcatgtgc
ag629	cgaatgacaaggcactgaaagggtgacagctattgggtctttg
ag630	tccagagtactgcccgctgccgaaaggcctttctcatgtgc
ag631	acatgaagaaagcccttccgagcgggcagctactc
ag632	aagaccaatagctgtcaccctttagtgcctgtcattcgg
ag633	cgaatgacaaggcactgaaagagcatgttcctttggc
ag634	tccagagtactgcccgctgccaccctttcacaagacc
ag635	gggtctttgtaaacgggtgccagcgggcagctactc
ag636	ctgcaaaggcaacatgctctttagtgcctgtcattcgg
ag637	ttgtgaacgggtgaaccctgaacatgaattcgaactgtcag
ag638	aaggcaacatgctccaccagaattgattttgaaccacttatcaaac
ag639	tcaaaaatccaattctgggtggagcatgttcctttggc
ag640	aaatcatgttcagcgggtcaccctttcacaagacc
ag641	agaaagcccttccaaccgctgaacatgaattcgaactgtcag
ag642	caatagctgtcaccaccagaattgattttgaaccacttatcaaac

ag643	gttcaaaaatccaattctgggggtgacagctattgggtcttg
ag644	gaaattcatgttcagcgggttgaaagggcttctcatgtgc
ag704	Gagcatgtgcctttggc
ag731	ggcggaggcggaaagcggcggaggcggatccggcggaggcggaaagccagtttataccgtaagtctggc
ag732	gcttccgctcccgccggatccgcctccgcttccgctccgctggcagtggtgggtgc
ag804	gcagccatatggctagcatggacagctattgggtctttgtgaaac
ag910	caaaggcaacatgctctggtggttcagtgcttgcattcgg
ag1046	Aagacaatacacgttccgtagtcac
ag1047	Cttcatttctgcaacgctgagtc
ag1048	ctcagcgttcagaaatgaagggtgacagctattgggtcttg
ag1049	ctacggaacgtgtattgtcttgaaagggcttctcatgtgc
ag1050	ctacggaacgtgtattgtcttaccggcttcacaaagacc
ag1051	ctcagcgttcagaaatgaaggagcatgttgcctttggcag
ag1052	Atagactttaaagagctgaactcgc
ag1058	Ggactgcaaccttctgtcc
ag1059	cggaacgaaggtgcagtcacaaagggagcatgttgcctttggc
ag1060	gttcagctctttaaagtctataccgagcaccggcttcacaaagacc
ag1061	cggaacgaaggtgcagtcacaaaggggtgacagctattgggtcttg
ag1062	gttcagctctttaaagtctataccgagggaagggcttctcatgtgc
ag1259	cagcgttcagaaatgaagggtgacagataatgggtctttgtg
ag1260	cggaaacgtgtattgtcttgaaagggcttcttcaagtc
ag1566	ggatccccctccgctgcccctcctccggactgtacagctcgtccatgcc
ag1703	Caatgcgagttcagctctttaaagtc
ag1704	ctttaaagagctgaactcgattgaaaaaggctatgaataagctcagcgttcagaaatgaag

Table S8. Plasmids used in this study

Plasmid	ORF
pAG399	His-FAST
pAG400	His-cpFAST2
pAG401	His-Kbp
pAG402	His-GltI
pAG403	His-cpGltI
pAG441	His-K ⁺ -FAST-1
pAG442	His-K ⁺ -FAST-2
pAG443	His-K ⁺ -FAST-3
pAG444	His-K ⁺ -FAST-4
pAG445	His-Glu-FAST-1
pAG446	His-cpGlu-FAST-1
pAG447	His-Glu-FAST-2
pAG448	His-cpGlu-FAST-2
pAG449	His-Glu-FAST-3
pAG450	His-cpGlu-FAST-3
pAG451	His-Glu-FAST-4
pAG452	His-cpGlu-FAST-4
pAG512	His-K ⁺ -FAST-5
pAG513	His-Glu-FAST-2-CFAST(116-125)
pAG625	His-K ⁺ -FAST-5.1
pAG634	His-Glu-FAST-2.1
pAG729	His- <i>B</i> .PS3
pAG733	His-ATP-FAST-1
pAG734	His-ATP-FAST-2
pAG735	His-ATP-FAST-3
pAG736	His-ATP-FAST-4
pAG881	His-ATP-pFAST-1
pAG1008	His-mCherry-ATP-pFAST-1
pAG1021	His-mCherry-ATP-FAST-1
pAG1091	His-ATP-FAST-1-R122K/R126K
pAG1092	His-ATP-pFAST-1-R122K/R126K

Supplementary References

- (1) Gibson, D. G.; Young, L.; Chuang, R.-Y.; Venter, J. C.; Hutchison, C. a; Smith, H. O.; Iii, C. A. H.; America, N. Enzymatic Assembly of DNA Molecules up to Several Hundred Kilobases. *Nat Methods* **2009**, *6* (5), 343–345. <https://doi.org/10.1038/nmeth.1318>.
- (2) Plamont, M.-A.; Billon-denis, E.; Maurin, S.; Gauron, C.; Pimenta, F. M.; Specht, C. G.; Shi, J.; Pan, B.; Rossignol, J.; Morellet, N.; Lescop, E.; Chen, Y.; Triller, A.; Saux, T. Le; Jullien, L.; Gautier, A. Small Fluorescence-Activating and Absorption-Shifting Tag for Tunable Protein Imaging in Vivo. *Proceedings of the National Academy of Sciences* **2016**, *113* (10), 497–502. <https://doi.org/10.1073/pnas.1602162113>.
- (3) Li, C.; Plamont, M. A.; Sladitschek, H. L.; Rodrigues, V.; Aujard, I.; Neveu, P.; Le Saux, T.; Jullien, L.; Gautier, A. Dynamic Multicolor Protein Labeling in Living Cells. *Chem Sci* **2017**, *8* (8), 5598–5605. <https://doi.org/10.1039/c7sc01364g>.
- (4) Benaïssa, H.; Ounoughi, K.; Aujard, I.; Fischer, E.; Goïame, R.; Nguyen, J.; Tebo, A. G.; Li, C.; Le Saux, T.; Bertolin, G.; Tramier, M.; Danglot, L.; Pietrancosta, N.; Morin, X.; Jullien, L.; Gautier, A. Engineering of a Fluorescent Chemogenetic Reporter with Tunable Color for Advanced Live-Cell Imaging. *Nature Communications* **2021**, *12* (1), 6989. <https://doi.org/10.1038/s41467-021-27334-0>.
- (5) Velazquez-Campoy, A.; Goñi, G.; Peregrina, J. R.; Medina, M. Exact Analysis of Heterotropic Interactions in Proteins: Characterization of Cooperative Ligand Binding by Isothermal Titration Calorimetry. *Biophys J* **2006**, *91* (5), 1887–1904. <https://doi.org/10.1529/biophysj.106.086561>.
- (6) Tebo, A. G.; Pimenta, F. M.; Zoumpoulaki, M.; Kikuti, C.; Sirkia, H.; Plamont, M.-A.; Houdusse, A.; Gautier, A. Circularly Permuted Fluorogenic Proteins for the Design of Modular Biosensors. *ACS Chem Biol* **2018**, *13* (9), 2392–2397. <https://doi.org/10.1021/acscchembio.8b00417>.